



---

**Innovations Deserving  
Exploratory Analysis Programs**

***Highway IDEA Program***

---

*A Study of Concrete Bridge Columns Using Innovative  
Materials Subjected to Cyclic Loading*

Final Report for Highway IDEA Project 116

Prepared by:

M. Sadrossadat-Zadeh, Melissa O'Brien and M. Saiid Saiidi, University of Nevada, Reno

***May 2007***

---

**TRANSPORTATION RESEARCH BOARD**  
*OF THE NATIONAL ACADEMIES*



**INNOVATIONS DESERVING EXPLORATORY ANALYSIS (IDEA)  
PROGRAMS  
MANAGED BY THE TRANSPORTATION RESEARCH BOARD (TRB)**

This NCHRP-IDEA investigation was completed as part of the National Cooperative Highway Research Program (NCHRP). The NCHRP-IDEA program is one of the four IDEA programs managed by the Transportation Research Board (TRB) to foster innovations in highway and intermodal surface transportation systems. The other three IDEA program areas are Transit-IDEA, which focuses on products and results for transit practice, in support of the Transit Cooperative Research Program (TCRP), Safety-IDEA, which focuses on motor carrier safety practice, in support of the Federal Motor Carrier Safety Administration and Federal Railroad Administration, and High Speed Rail-IDEA (HSR), which focuses on products and results for high speed rail practice, in support of the Federal Railroad Administration. The four IDEA program areas are integrated to promote the development and testing of nontraditional and innovative concepts, methods, and technologies for surface transportation systems.

For information on the IDEA Program contact IDEA Program, Transportation Research Board, 500 5<sup>th</sup> Street, N.W., Washington, D.C. 20001 (phone: 202/334-1461, fax: 202/334-3471, <http://www.nationalacademies.org/trb/idea>)

The project that is the subject of this contractor-authored report was a part of the Innovations Deserving Exploratory Analysis (IDEA) Programs, which are managed by the Transportation Research Board (TRB) with the approval of the Governing Board of the National Research Council. The members of the oversight committee that monitored the project and reviewed the report were chosen for their special competencies and with regard for appropriate balance. The views expressed in this report are those of the contractor who conducted the investigation documented in this report and do not necessarily reflect those of the Transportation Research Board, the National Research Council, or the sponsors of the IDEA Programs. This document has not been edited by TRB.

The Transportation Research Board of the National Academies, the National Research Council, and the organizations that sponsor the IDEA Programs do not endorse products or manufacturers. Trade or manufacturers' names appear herein solely because they are considered essential to the object of the investigation.

**A Study of Concrete Bridge Columns Using  
Innovative Materials Subjected to Cyclic Loading**

Summary Report

M. Sadrossadat-Zadeh  
Melissa O'Brien  
M. Saiid Saiidi

A Report to NCHRP-IDEA

**Center for Civil Engineering Earthquake Research**  
Department of Civil and Environmental Engineering/258  
University of Nevada  
Reno, NV 89557

January 2007



## **Abstract**

In an attempt to improve performance of concrete bridge columns subjected to strong earthquakes, three 0.2 scale circular columns using innovative materials in the plastic hinge zone were tested under cyclic loading. The first column (RSC) utilized conventional concrete and steel reinforcement, the other two (RNC and RNE) incorporated shape memory alloy (SMA) longitudinal reinforcement, and the third (RNE) utilized engineered cementitious composites (ECC) in the plastic hinge.

The average ratio of residual to maximum displacement in RSC, RNC, and RNE was 0.82, 0.27 and 0.14, respectively, indicating substantial benefits of using innovative materials. RNE experienced the least damage and highest drift capacity among the three columns. The test results showed that SMA and ECC are very effective in improving serviceability of bridges after earthquakes.

Analytical studies using the program OpenSees led to reasonable estimates of residual drifts, overall cyclic response, and forces when compared to the experimental results.



## **Acknowledgements**

This study was funded by the National Cooperative Highway Research Program (NCHRP) Innovations Deserving Experimental Analysis (IDEA) initiative. The support and guidance of Dr. Inam Jawed of the NCHRP-IDEA is greatly appreciated. The authors would like to acknowledge Mr. Edward R. Little of Surface Systems Incorporation for his assistance regarding the ECC mix design, construction, and SMA removal. Dr. Darel Hodgson of Nitinol Technology Incorporation is thanked for his insight into the performance of shape memory alloys and the manufacturing of the bars used in this study. The authors would like to thank Dr. Patrick Laplace, Mr. Paul Lucas, and Mr. Tim Steele for their help in constructing and testing the column materials and specimens. Additionally, for their assistance in constructing the specimens, a word of gratitude goes to Mr. Edgar Gabriel, Mr. David Hillis, Mr. Hoon Choi, Mr. Robert Nelson, Mr. Michael Taylor, Mr. Neil Bahen, Mr. Zhi-yuan Cheng, Mr. Shenlin Lu, Mr. Chad Lyttle, and Mr. Nick Maxon.





## TABLE OF CONTENTS

<b>ABSTRACT .....</b>	<b>i</b>
<b>ACKNOWLEDGEMENTS .....</b>	<b>ii</b>
<b>TABLE OF CONTENTS .....</b>	<b>iii</b>
 <b>1. Introduction</b>	
1.1. Background .....	1
1.2. Literature Review .....	3
1.3. Objectives and Scope .....	3
<b>2. Background and Discussion of SMA and ECC</b>	
2.1. Introduction .....	4
2.2. Shape Memory Alloys .....	4
2.3. Engineered Cementitious Composites .....	5
<b>3. Test Specimens and Experimental Set-Up</b>	
3.1. Introduction .....	7
3.2. Selection of Test Specimens .....	7
3.3. Design of Test Specimens .....	7
3.3.1. Column and Loading Head .....	7
3.3.2. Footing .....	8
3.3.3. Plastic Hinge Zone .....	8
3.4. Material Properties .....	9
3.4.1. Reinforcement .....	9
3.4.2. ECC and Conventional Concrete .....	9
3.5. Instrumentation .....	10
3.6. Test Setup .....	11
3.7. Cyclic Loading Program .....	12
<b>4. Experimental Results</b>	
4.1. Introduction .....	13
4.2. RSC .....	13
4.2.1. General Observations .....	13
4.2.2. Forces and Displacements .....	13
4.3. RNC .....	14
4.3.1. General Observations .....	14
4.3.2. Forces and Displacements .....	15
4.4. RNE .....	16
4.4.1. General Observations .....	16
4.4.2. Forces and Displacements .....	16
4.5. Performance Comparison .....	17
4.5.1. General Observations .....	17
4.5.2. Residual Drift .....	18
4.5.3. Forces and Displacements .....	18
4.5.4. Energy Dissipation .....	19
4.5.5. SMA Properties After Column Tests .....	20
<b>5. Analytical Studies</b>	
5.1. Introduction .....	21
5.2. Model Method .....	21
5.3. Pushover Analysis .....	23
5.3.1. RSC .....	23



5.3.2. RNC.....	24
5.3.3. RNE.....	25
5.4. Cyclic Loading Analysis.....	25
5.4.1. RSC .....	25
5.4.2. RNC.....	26
5.4.3. RNE.....	26
<b>6. Summary and Conclusions</b> .....	
6.1. Summary .....	27
6.2. Conclusions.....	28
<b>References</b> .....	30
<b>Tables</b> .....	33
<b>Figures</b> .....	38
<b>Appendix A: Cost Comparison for Bridges with Conventional and Innovative Materials</b> .....	53



## **Chapter 1**

### **Introduction**

#### **1.1 Background**

Current seismic design practice for reinforced concrete columns focuses on yielding steel when the structure is subjected to large lateral loads in order to dissipate energy. This causes large permanent displacements and makes the structure susceptible to severe damage. In standard, non critical structures, damage to plastic hinge is an accepted practice to allow for energy dissipation. However, the consequence of this damage can interfere with disaster recovery operation and can have major economic impact on the community. Column plastic hinges that can dissipate energy without experiencing severe damage and permanent deformation would alleviate these problems. This study focused on ductile columns that experience substantially reduced damage and permanent deformation while dissipating the earthquake energy under severe seismic loading. Two innovative materials that are relatively new to civil infrastructures were incorporated in column plastic hinges: superelastic shape memory alloy (SMA) reinforcement and engineered cementitious composites (ECC), which is essentially a type of concrete.

Superelastic shape memory alloys are able to undergo large levels of strain (up to 8%) and still recover their shape through either heating (shape memory effect) or stress removal<sup>1</sup>. The behavior of SMA is a function of temperature, stress, and strain. In this study, the super-elastic behavior of NiTi (Nitinol: 55.9% Nickel, 44.1% Titanium), one of the most often used SMA, was explored.

Another issue that arises during earthquakes is the brittleness of conventional concrete and its low capacity in tension. The replacement of conventional concrete by ECC at the column plastic hinge could improve the column behavior under earthquake loads. ECC is a fiber-reinforced cement-based composite engineered for high tensile ductility, and high compressive and tensile strength. This study investigated the use of ECC with 2% synthetic poly-vinyl-alcohol (PVA) fiber content by volume.

The combination of the low deformability of ECC with the superelastic characteristics of NiTi offers great potential of increasing ductility, and decreasing damage and residual displacements of concrete members under cyclic loads. Three concrete bridge column specimens were tested in this study to investigate the possible use of NiTi and ECC. In addition, extensive analytical studies were conducted to explore modeling methods that would estimate the response with reasonable accuracy.

#### **1.2 Literature Review**

There is limited research up to now on the use of either SMA or ECC in the plastic hinge region of reinforced concrete columns subjected to seismic loads, especially when used in combination. Also, little research has been directed towards understanding the ability of SMA to recover deformations and decrease residual deformations in concrete structural elements. Some research has explored the possibility and efficiency

of using SMA as restrainers or connections, while others utilized SMA in structural control.

Since the introduction of ECC material about a decade ago, it has undergone major evolution in both material development and range of emerging applications. Some of the research has focused on the unique properties of ECC to contribute to repair and retrofit of structures, while others investigated the replacement of conventional concrete with ECC to reduce residual displacements. The most relevant literature reviews about SMA and ECC to the current study are presented.

Studies on different potential applications of SMA have been reported in the literature. They included the use of SMA for structural vibration control<sup>2</sup>, to retrofit historical monuments<sup>3</sup>, to reduce permanent deformation of concrete beams<sup>4,5</sup>, to improve steel column-beam connections<sup>6</sup>, and to pre-stress concrete<sup>7</sup>. A study on cyclic properties of SMA wires<sup>8</sup> showed that nearly ideal super-elastic properties can be obtained in both the wire and bar and the re-centering capabilities (based on residual strains) are not affected by section size.

The use of ECC in repair and retrofit of concrete structures<sup>9</sup> showed a unique damage tolerant behavior of ECC to make it a suitable material for seismic retrofit applications. The combination of a ductile cementitious matrix and steel reinforcement resulted in improved energy dissipation capacity, reduction of transverse steel reinforcement requirements, and damage-tolerant inelastic deformation behavior for the member<sup>10</sup>. Test results on small-scaled specimens indicated advantageous synergistic effects between ECC matrix and steel reinforcement with respect to compatible deformation, structural composite integrity, and damage evolutions<sup>14</sup>. The use of ECC with FRP was found to increase deflection capacity, reduce permanent deflections, and delay concrete failure in the columns<sup>11</sup>.

Relatively large elastic deflection capacity of the columns was achieved by combining FRP bars with ECC. ECC has considerably higher tensile and deformation capacity than normal concrete, thus the use of ECC with FRP was found to increase deflection capacity, reduce permanent deflections, and delay concrete failure in the columns<sup>11</sup>. In another study, the interaction of FRP reinforcement and ECC resulted in nonlinear elastic flexural response characteristics, stable hysteretic behavior, small residual displacements, and ultimately gradual compression failure<sup>12</sup>.

In a recent study at University of Nevada, Reno (UNR), shake table tests were conducted to determine the seismic performance of reinforced concrete columns with SMA longitudinal reinforcement in the plastic hinge area and to evaluate the effectiveness of SMA in reducing permanent column displacement<sup>13,14</sup>. Additionally, this study investigated the use of ECC as a repair material in the SMA reinforced column with respect to seismic performance and damage progression. Data from similar columns using conventional concrete and reinforcement were used to evaluate the effect of SMA and ECC in the plastic hinge region. Results from this study showed that SMA aided the column in recovery of deformations, and ECC substantially reduced the damage to the concrete. The conclusion was made that incorporating SMA and ECC into the plastic hinge region of columns would mean that minimal repairs would be necessary even after very large earthquakes. Because the loading was through shake table simulation with little control of maximum displacement amplitude, displacement recovery characteristics of SMA-reinforced columns could not be fully quantified. Furthermore, the use of ECC



in that study was limited to repair. The study did not allow for evaluation of performance of columns with full SMA/ECC combination in the plastic hinge.

### **1.3 Objectives and Scope**

The primary objective of this study was to investigate the cyclic performance of reinforced concrete columns with SMA longitudinal reinforcement and ECC in the plastic hinge region. The main focus was to evaluate the effectiveness of SMA and ECC in reducing permanent residual column displacements.

To achieve the objectives, three reinforced concrete columns were designed, constructed, and tested in the Large Scale Structure Laboratory of the University of Nevada, Reno. Aside from the type of reinforcement and concrete used, the three columns were identical. Further explanation of the columns is given in chapter 3. Comparisons of the test results were made among the three specimens, specifically with respect to residual drift vs. maximum column drifts, moment-curvature, force-displacement relationships, curvature and displacement ductility, and energy dissipation.

Analytical studies were then performed to investigate the ability of modeling the column behavior. Analytical models included moment curvature, pushover force-displacement relationship, and cyclic behavior of all three specimens. Additional computations were made from the model data to make comparisons among the three specimens with respect to residual drifts, ductility, and forces. Calculated and measured results were compared to evaluate the validity of the analytical models.

## Chapter 2

### Background and Discussion of SMA and ECC

#### 2.1 Introduction

Two columns in this study are constructed with materials that are fairly new to the field of structural engineering. Therefore, in order to properly evaluate the response of these columns, it is important to first understand the materials. This chapter focuses on Shape Memory Alloys (SMA) and Engineered Cementitious Composites (ECC) with respect to their history, important properties, and considerations necessary for this study. More discussion on the properties of SMA and ECC is presented in Ref. 15.

#### 2.2 Shape Memory Alloys

SMAs are a special class of alloys that have the ability to return to their original shape even after large deformations. Deformation recovery is accomplished through either removal of stress (superelastic effect) or by heat (shape memory effect). Therefore, the behavior of SMA is a function of temperature, stress, and strain as shown in Figure 2-1.

The first discovery of SMAs was in 1932; however, it was not until the 1960s that significant research took place, and then approximately twenty years passed before practical applications for SMAs were realized. One of the most popular SMAs, the binary NiTi alloy made of equi-atomic compositions of nickel and titanium, was discovered in 1962. NiTi is often referred to as “Nitinol,” an acronym for ‘Nickel Titanium Naval Ordinance Laboratory’ because it was developed at the U.S. Naval Ordinance Laboratory<sup>16</sup>. NiTi is the most popular SMA because of its high strength, large strain range, high resistance to fatigue and corrosion, and biocompatibility. NiTi applications include cell phone antennas, eye-glass frames, orthodontic wires, and medical devices. Some copper-based tertiary alloys are also used commercially, though they are less common and they have not been used for seismic applications<sup>1</sup>.

In general, SMAs exhibit two distinct crystal structures, or phases. These phases are ‘martensite’ and ‘austenite.’ Martensite has the ability to completely recover residual strains by heating, and austenite will have nominally zero residual strain when released following arbitrary mechanical loading of up to 10% strain<sup>17</sup>. During deformation SMAs pass through these two phases through shifts in the crystal structure whereas typical metals experience intergranular dislocations. Some terms must first be defined in order to understand this process.

Figure 2-1 shows how the behavior of the SMA material varies between certain temperatures. The austenite start temperature ( $A_s$ ) is the temperature at which the crystal structure begins to shift from martensite to austenite, and the austenite finish temperature ( $A_f$ ) is the temperature at which the material shift is complete and it is fully in the austenite phase. The martensite start temperature ( $M_s$ ) is when the material begins to shift from austenite to martensite, and the martensite finish ( $M_f$ ) is the temperature where the phase shift is complete and the material is fully in the martensite phase. The alloy exists in both the martensitic and austenitic phases while the temperature is between the ranges of  $A_s$  and  $A_f$ , and  $M_s$  and  $M_f$ .

The specimen begins in its austenite phase at a temperature above  $A_f$ . Upon loading and unloading the response of the specimen results in a flag-shaped hysteresis

loop with six definable regions (Figure 2-2). In the first region (for strains up to approximately 1%) the material behaves elastically, meaning that upon removal of the load the material will return to its undeformed shape. The second region (strains from approximately 1% to 6%) consists of a long and almost constant stress plateau (called the loading plateau) as strain increase and the phase transformation from austenite to stress induced martensite takes place. The third region (strains greater than 8%), elastic behavior of the martensite phase occurs. The fourth region begins once the stress is removed and the martensite experiences elastic recovery. The fifth region consists of recovery at another long and almost constant stress plateau (called the unloading plateau), but occurring at a lower level of stress than region two. Here, the material is transforming back into the austenite phase because stress induced martensite is unstable at temperatures above  $A_f$ . The sixth region is the elastic recovery of the austenite phase. If stress exceeds the elastic limit of the stress induced martensite in region three then plastic deformation will occur, producing residual strain. As displayed in Fig. 2-1, at temperatures greater than  $M_d$ , the material will remain in austenite phase and simply behave elastically in the first region followed by plastic deformation<sup>1</sup>.

The behavior of SMAs under cyclic loading is an important issue for their use in earthquake engineering. Studies have shown that for increasing stress induced strain both loading and unloading transformation stresses decrease, apparent in the downward shift of the stress-strain hysteresis loop while the thickness of the loop remains constant<sup>1</sup>. Also, it has been noted that residual strain gradually increases with repeated cycling caused by microstructural slips during the stress induced martensitic transformation<sup>9</sup>. Fatigue or the effect of cyclic degradation leads to lower energy dissipation capabilities and higher strain hardening. However, the degradation stabilizes after several initial cycles; therefore, pre-cycling, or training, of the SMA specimen could decrease the effects of fatigue<sup>18</sup>.

### 2.3 Engineered Cementitious Composites

ECC is a fiber-reinforced cement-based composite engineered for high tensile ductility, compressive, and tensile strength. ECC contains water, cement, fine sand, fiber, and some common chemical additives. Coarse aggregates are not used in the mix because they adversely affect the unique ductile behavior of the composite. The fibers are typically reinforced with Polyvinyl Alcohol fibers (PVA) or high modulus polyethylene fibers (PE).

ECC was developed in the early 1990's to counteract some of the disadvantages of conventional concrete including brittle failure under severe loading, deterioration under service loads, and lack of sustainability of conventional reinforced structures as indicated by necessary and repeated repairs. Therefore, ECC has been designed to be a highly ductile, durable, and sustainable material.

Although ECC is a relatively new material, it has already found useful applications in the field of civil engineering, and uses are expanding. For example, in Hokkaido, Japan the Mihara Bridge uses a steel/ECC composite deck, and in Hiroshima, Japan, ECC is being used for the repair of the Mitaka Dam. A field study on the long term behavior of ECC is being conducted on a concrete gravity earth retaining wall that was damaged by alkali-silica reaction cracking. The damaged wall was repaired with

both conventional concrete and ECC for comparison purposes. Ten months after the repair the conventional concrete crack width was 0.2 mm (0.0079 in.) while the ECC crack were less than 50 $\mu$ m (0.002 in.) wide<sup>19</sup>.

First, it is important to understand the physical properties of ECC, and then the concepts behind the material development can be discussed. ECC has the ability to reach ultimate tensile strain of approximately 3% to 5%<sup>20</sup>. This high strain capacity is nearly 500 times larger than that of conventional concrete or fiber reinforced concrete (FRC), and can be attributed to the strain-hardening behavior and unique cracking mechanism<sup>21</sup>. A typical uniaxial tension stress strain curve with cracking behavior of ECC is shown in Figure 2-3. Many thin and closely spaced microcracks form as tensile load is applied, whereas conventional concrete and FRP accommodate deformations by the widening of cracks. The microcracks carry increasing load similar to strain-hardening of ductile metals because of the bridging mechanism of the fibers across the crack opening. Therefore, the small crack width (less than 200 $\mu$ m (0.0079 in.)) and tight spacing (0.5 to 5 mm (0.02in to 0.2in)) is a property of the material itself and not dependant on reinforcement or the size of the structure<sup>10</sup>.

In systems of ECC reinforced with steel, the load carrying capacity of the ECC cracks prevents the tension from being transferred to the steel. Since no force is transferred, very little shear stress develops thus no cracking or debonding occurs at the ECC-reinforcement interface. Once the tensile strain carrying capacity of ECC has been reached, the structure will have likely reached its serviceability limit state. For this reason, the ECC load carrying capacity can possibly reduce the amount of required reinforcement, especially for shear<sup>21</sup>.

Figure 2-4 shows a typical stress strain curve comparing conventional concrete to ECC in compression. ECC reaches its maximum compressive strength at higher strains compared to conventional concrete due to its lack of coarse aggregates. The lack of coarse aggregate is also reflected in the lower modulus of elasticity (smaller initial slope) in the ECC stress-strain diagram.

## **Chapter 3**

### **Test Specimens and Experimental Procedure**

#### **3.1 Introduction**

The focus of this study was on the cyclic performance of reinforced concrete bridge columns using innovative materials. Two parameters were varied among three columns. The first was the longitudinal reinforcement using steel versus shape memory alloys (SMA). The second was utilizing conventional concrete versus engineered cementitious composites (ECC).

This chapter describes the test specimen design and construction, material properties, instrumentation, experimental setup, and the testing program.

#### **3.2 Selection of Test Specimens**

Three 0.2 scale reinforced concrete bridge columns with circular sections were investigated in this study. The first column, which served as a reference, incorporated conventional concrete and steel reinforcement. It is referred to as RSC, for “Round Steel Conventional concrete.” The second column incorporated conventional concrete and NiTi for longitudinal reinforcement in the plastic hinge region. This column is called RNC for “Round NiTi Conventional concrete”. The third column was similar to RNC, but the conventional concrete was replaced with ECC in the plastic hinge region. This column is referred to as RNE for “Round NiTi Engineered cementitious composites.”

SMAs are very expensive, but the Nitinol (NiTi) selected for this study is one of the least expensive types of SMAs due to its availability and the relatively high demand in non-civil engineering applications. NiTi was also chosen because of its relatively low and stable transformation temperatures, which are ideal for field conditions.

ECC is a high performance fiber-reinforced cementitious composite designed based on micromechanical principles. ECC exhibits superior tensile strength compared to conventional concrete with a tensile strain-hardening behavior. In this study, polyvinyl alcohol (PVA) fibers were selected for the mix in ECC.

#### **3.3 Design of Test Specimens**

Flexure dominates the behavior of typical bridge columns. Thus, to ensure this behavior and to avoid shear failure an aspect ratio of 4.5 was selected. The dimensions of the columns were 10 in. (254 mm) diameter and 45 in. (1143 mm) height from the top of the footing to the centerline of the lateral load. The clear height of the columns was 35 in. (889 mm) since lateral load was applied at the center of a 20 in. (508 mm) cubic loading head.

##### **3.3.1 Column and Loading Head**

Figure 3-1 shows the column details. Each column was reinforced with 8 longitudinal bars evenly spaced in a circular pattern corresponding to 2% longitudinal reinforcement ratio. The longitudinal bars extended from the top of the head through the column and were fully developed in the footing.

RSC was reinforced with #4 (Ø12.7mm) Grade 60 (414MPa) steel. RNC and RNE were reinforced with 0.5 in. (12.7 mm) diameter NiTi rods in the plastic hinge zone and #5 (Ø15.9 mm) Grade 60 (414 MPa) steel through the remainder of the column length.

Figure 3-2 shows the cross sections of the columns. The column concrete clear cover was specified at 0.5 in. (12.7 mm) in RSC. The clear cover in RNC and RNE was 0.5 in. (12.7 mm) only at the couplers, but increased to 0.63 in. (16 mm) at the #5 steel longitudinal reinforcement and 0.69 in. (17.5 mm) around the SMAs. This change in clear cover was due to the smaller diameter of the longitudinal bars and SMAs compared to the couplers. The transverse spiral reinforcement was designed using the NCHRP 12-49 provisions<sup>22</sup>.

A concrete clear cover of 1 in. (25.4 mm) was used for the column head. Minimal reinforcement was needed in the loading head since it was subjected to little stress. Four loops of #4 ( $\varnothing$  12.7 mm) bars were placed evenly in horizontal layers to confine the concrete. Four 2 in. (50.8 mm) inner diameter PVC pipes were cast in the head to accommodate the rods used to secure the actuator to the column.

### 3.3.2 Footing

The footing was designed to be strong and stiff in order to avoid damage and shear failure, and to resist overturning moments. The height of the footing was selected based on the level of the actuator which was secured through available hole locations in the strong wall. The footing plan view dimensions were 60 in. (1524 mm) by 28 in. (711.2 mm) and the depth was 30 in. (762 mm). The clear cover of the footing was 1.5 in. (38.1 mm) all around. Four #8 ( $\varnothing$  25.4 mm) bars were used in the long direction and six #8 ( $\varnothing$  25.4 mm) bars were used in the short direction. Identical bottom and top steel mats were placed to resist positive and negative moments. Two 3 in. (76.2 mm) inner diameter PVC pipes were cast for passage of the anchor rods through the footing to the strong floor.

### 3.3.3 Plastic Hinge Zone

RNC and RNE were designed to evaluate the effect of using NiTi and ECC, but to minimize cost, these material were only used in the plastic hinge zone. A plastic hinge length of 8.1 in. (205.7 mm) was calculated according to Paulay and Priestley's equation and based on the SMA specified yield strength of 60 ksi (413.7 MPa)<sup>23</sup>. The NiTi rods were designed based on this length, and identical to SMA rods used in a previous study<sup>13</sup>.

Figure 3-3 shows the plastic hinge detail for RNC and RNE. The total length of the NiTi rods was 14 in. (355.6 mm). They extended 10 in. (254 mm) from the top of the footing to the middle of the upper coupler, and 4 in. (101.6 mm) from the top of the footing to the middle of the lower coupler. The middle 8 in. (203 mm) of the rod had a diameter of 0.5 in. (12.7 mm) to correspond to the diameter of the #4 steel rebar used in RSC. On either side of the rods, the diameter was increased to 5/8 in. (15.9 mm) over transition length of 3/16 in. (4.8 mm). This diameter increase was necessary to force yielding in the middle portion of NiTi and to prevent stress concentration in the threads. Each end was threaded over a length of 2.125 in. (54 mm) with 5/8-11 National Coarse (NC). The couplers used to connect the NiTi to the steel were 7/8 in. (22.2 mm) in diameter and 2 in. (50.5 mm) in length. Figure 3-4 shows the NiTi rod detail. Figure 3-5 is a photo of the steel-NiTi connection above and below the plastic hinge region.

In RNE, ECC was incorporated in the plastic hinge zone in order to evaluate the combined performance of the two innovative materials. The height of the ECC was 20 in. (508 mm). This height extended above the plastic hinge region to avoid weakened



capacity at the material interface in the plastic hinge zone and at the NiTi-steel connection.

### **3.4 Material Properties**

#### **3.4.1 Reinforcement**

Table 3-1 shows the tensile test results from one NiTi rod, two #4 ( $\varnothing$  12.7), two #5 ( $\varnothing$  15.9 mm) longitudinal bars, and two spiral wires. All material properties were the same among the three columns since the steel came from the same batch, the wire from the same roll, and the SMAs were produced all at one time. Grade 60 (413.7 MPa) steel was specified but the actual bars exhibited higher yield stresses. On the other hand, a yield point between 60 ksi (413.7) and 70 ksi (482.6 MPa) was requested for the SMAs, but they ended up with a yield stress of approximately 55 ksi (379.2 MPa). The measured average elastic modulus of the SMA found from the strain gage data and the laser reading was 9136 ksi (62990 MPa). The SMA yield point was obtained from both the laser and strain gage measurements using the 0.2% rule. The method of the 0.2% rule is to draw a line from 0.2% strain point (at zero stress) parallel to the initial tangent to the curve (that is, the elastic modulus 'E line'). The yield stress is read at the intersection point of the 0.2% line and the measured stress strain curve. Figure 3-6 shows the stress strain curves and lines used for the 0.2% rule from the NiTi tensile test using a laser transducer. The reason for the low yield in the SMAs is a result of the heat treatment and machining process necessary to manufacture the rods.

#### **3.4.2 ECC and Conventional Concrete**

The three specimens had the same concrete properties since they were built simultaneously in two stages. First, the formwork for the footing was built, the footing and column reinforcement cages were placed, and then footing concrete was poured. Next, in RNE the formwork for the ECC portion was built, and the ECC poured. The ECC was mixed, poured in 5 lifts (all from the same mix), and vibrated after each lift. While the ECC was curing, the columns (including the top 15 in. (381 mm) of RNE) and the head formwork were built. Concrete for the head and columns was poured at one time for all three specimens. This construction method left only one cold joint at the footing column interface for RSC and RNC, and an additional cold joint at the ECC-conventional concrete interface in RNE. The surfaces at these joints were left rough after each pour to allow for a better bond.

The maximum aggregate size for the conventional concrete was 0.375 in. (9.525mm). Slump was measured before the concrete was poured. For the footing, the slump was 4 in. (101.6 mm) and for the column it was 3 in. (76.2 mm). Table 3-2 shows the results from the 7, 28, and test day cylinder compression tests. A total of fifteen 6 in. (152.4 mm) by 12 in. (304.8 mm) cylinders were tested for both the column and footing concrete. The strength of the column cylinders decreased after RSC test day. This unusual strength decrease can be attributed to the quality of the cylinders made on the casting day. Cylinders were made using the standard method of pouring three separate lifts and tamping between each one to consolidate and decrease air voids. However, not all cylinders were properly tamped, thus many had large divots and air voids. Additionally, the truck ran out of concrete after all the columns and heads were poured, but two cylinders still needed concrete to fill the third lift. Since the truck was out of

concrete a small batch of concrete that had been slump tested before the pour was used to fill these two cylinders. This last bit of concrete had only approximately 1.75 in. (44mm) slump. These two cylinders were tested at 7-days. The best cylinders were saved for the 28 day tests. Therefore, for all calculations in the following chapters, the 28 day strength is used for conventional concrete.

Table 3-3 lists the mix design for the ECC. The percentages listed in this table are by weight. For the ECC mix, PVA (polyvinyl alcohol) fibers were used. The mix contains 1.35% fiber by weight, which is equivalent to 2% by volume. HPMC stands for "Hydroxy propyl methel celulos" and it is a type of water reducer. The mix was prepared before the day of casting, and then the water was added to the mix just before the pour. Therefore, the ingredients used were dry applied materials, including the super-plasticizer. The water-cement ratio was 0.68 and water-cement plus fly ash ratio was 0.34.

Ten 3 in. (76.2 mm) by 6 in. (152.4 mm) ECC cylinders were made for the compression tests. The small cylinder size was selected to minimize cost. Table 3-2 shows the results from the ECC compression tests. Fly ash, which was used in the ECC mix, delays the strength gain of cementitious material in early ages. This caused a relatively low compressive strength at seven days, but there was significant strength gain observed in the twenty-eight day and test-day specimens. The test day results for ECC are used for all calculations in the following chapters.

ECC is unique due its high tensile strength and strain capacity. Two types of tests were performed on the ECC in order to determine the tensile strength of the mix used in this study. The first, the beam flexure test, is for determining the modulus of rupture and represents the performance of ECC in flexure. This test was important since RNE would be subjected to flexure. The second test, direct tensile test, was used to show the behavior of ECC under pure tension. Nine 1 in. (25.4mm) by 1 in. (25.4 mm) by 5 in. (127 mm) beams were made for the beam flexure test. Beam flexure tests were performed at 28 days and on the test day.

Eight dog bone coupon specimens were made for ECC direct tensile tests. The coupons had to be saw cut into thin strips to fit into the testing device. It is likely that micro-cracks formed in the samples during this cutting, and the edges were not perfectly level. The results from the coupon tests came out extremely low and not representative of the true ECC strength. Therefore, these test results were neglected in all analysis.

### **3.5 Instrumentation**

A variety of instruments were attached internally and externally to record the response of the columns. The three columns had the same instrumentation plan to facilitate comparisons of the response. Thirty TML YFLA-2-5L strain gauges were attached to the column reinforcement in each specimen. The strain gauges started at 5.5 in. (139.7 mm) below the footing column interface and were extended to 16.5 in. (419.1 mm) above the footing at uneven intervals. Twelve strain gauges were attached to the spirals and 18 were on the longitudinal reinforcement. In RNC and RNE, 12 strain gauges were on the NiTi and the other six were on the steel. The strain gauge wires were protected in plastic tubes and routed down the column and through the footing.

Lateral forces were measured by a bridged load cell between the actuator swivel and shaft. The axial load was measured by load cells between hydraulic rams and the

spreader beam attached to the head. Column displacements were controlled by the actuator.

### 3.6 Test Setup

Figure 3-7 shows a photo of the test setup of RNC. The setup for RSC and RNE was similar. Static cyclic testing was conducted on all three columns in the Large Scale Structures Laboratory at UNR. The specimens were lifted and centered in place onto 0.5 in. (12.7 mm) wood blocks. The footing was loosely secured to the 3 foot (.91 m) deep strong floor with two 1.25 in. (31.75 mm) Dywidag<sup>TM</sup> post tensioning bars passing through the PVC pipes in the footing. Formwork was placed around the base of the footing and hydrostone was poured in the gap between the footing and the floor to create a level surface. After the hydrostone cured, the Dywidag<sup>TM</sup> bars were tensioned to 100 kips (444.82 kN).

A steel spreader beam was bolted to the top of the column heads to distribute the axial load provided by hydraulic rams. Two 1.25 in. (31.75 mm) Dywidag<sup>TM</sup> were used to attach the spreader beam, rams, and load cells to the strong floor. Typically, bridge columns have an axial load index (ALI) of 0.05 to 0.1, defined as

$$ALI = \frac{P}{f'_c \cdot A_g} \quad (3.3)$$

Where:

ALI = axial load index

P = axial load

$f'_c$  = specified compressive strength of concrete at 28 days

$A_g$  = gross area of column

An ALI of 0.1 was selected, corresponding to an axial load of 35.34 kips (157.2 kN) (based on specified conventional concrete  $f'_c$  of 4.5 ksi (31.03 MPa). This load was monitored and kept relatively constant through out the tests by connecting the hydraulic system to an accumulator.

A strong wall was made from a stack of four 4 feet by 4 feet by 8 feet (1.22 m by 1.22 m by 2.44 m) concrete blocks that were tensioned to the floor with Dywidag<sup>TM</sup> bars. A steel plate with holes to attach the actuator was fastened with Dywidag<sup>TM</sup> bars running horizontally through the concrete blocks. The steel plate had to be extended out 17 in. (431.8 mm) from the face of the strong wall; therefore, eleven steel blocks (6 in. by 7 in. by 1.5 in. (152.4 mm by 177.8 mm by 38.1 mm)) were placed on each Dywidag<sup>TM</sup> bar before the plate was lifted. A 110 kip (489.3 kN) actuator was bolted on one side to the steel plate. The other side of the actuator was attached by means of Dywidag<sup>TM</sup> bars passing through the PVC pipe in the column head and bolted on both sides.

The columns were painted a light white with lime so that cracks would be more visible. The Novotechnik transducers were put on to the all thread rods, and all instruments were connected to the data acquisition system. All instruments were checked for functionality prior to testing.

### 3.7 Cyclic Loading Program

In static cyclic tests, it is common to use a cyclic program based on ductility; however, the unknown behavior of SMA and ECC made it difficult to estimate ductility of the columns. Therefore, the loading plan was determined based on drift ratio

(displacement at the top of the column divided by the total column height, taken from the top of the footing to the center of the loading head).

Figure 3-8 shows the cyclic load plan for the static tests. The cycles started at very low drifts so that initial behavior could be easily monitored. Also, there was a chance that RNE would exhibit higher initial capacity due to the high tensile strength of ECC. To capture this possible behavior, one cycle was made at 0.25% drift, two cycles at 0.5%, 1.0% and 1.5% drifts. Then 1% increments started at 2% drift up to failure. During the first column test (RSC), it was decided that 6%, 8% and 9% drifts could be skipped without harm to behavior analysis. These drifts were also skipped for RNC and RNE to keep consistency among the three test specimen. RNE reached higher drifts; therefore 11% and 13% drifts were also skipped. Table 3-4 shows the actual cycle numbers and drifts reached. The highlighted values represent residual drift where the columns were stopped at zero load.

The load rate of RSC was 0.01 in/second (0.254 mm/second) from the start until 3% drift. At 3% drift the load rate was changed to 0.02 in/second (0.508 mm/second). The load rate of RNC and RNE was 0.02 in/second (0.508 mm/second) up to 1% drift, and then at 1% drift the load rate was changed to 0.04 in/second (1.016 mm/second). For all practical purposes these rates are essentially near static.

## **Chapter 4**

### **Experimental Results**

#### **4.1 Introduction**

This chapter discusses the experimental results of the cyclic loading tests of the three columns. The results include general observations of the column performance, forces, and moments, strains, and curvatures. Also, the performances of the columns are compared and the effects of different test parameters are discussed.

#### **4.2 RSC**

##### **4.2.1 General Observations**

Throughout this document, the direction of testing will be referred to as positive or to the east for when the column was being pushed, and negative or to the west for when the actuator was pulling the column.

The concrete cover began to spall on the east side after the first run to positive 3% drift. The spiral was first exposed on the east side of the column after reaching the second excursion to negative 3% drift, and on the west side after the second cycle to positive 4% drift. At this point it became apparent that the column clear cover was different on the east and west side because the column form had not been fully centered around the reinforcement cage. The measured depth of concrete cover was 0.9 in. (22.9 mm) on the west side while it was only 0.4 in. (10.2 mm) on the east side. As will be discussed more in depth in the following paragraphs, this difference affected the response in the east as compared to the west direction.

Spalling continued, exposing more spiral bars, especially on the east side. The first longitudinal reinforcement was slightly visible on the west side after the first push to 5% drift and on the east side after the first pull to negative 5% drift. Just after the first push to 7% drift damage in the core concrete began to become evident. At this drift, a total of three spirals and one longitudinal bar were visible on the west side, and five spirals and two longitudinal bars were exposed on the east side. Cracking and slight spalling could be seen at a small depth into the core concrete by the first cycle to positive 10% drift. Two longitudinal bars on the west side buckled after the first pull to negative 10% drift. When the column was pushed back to the second cycle at positive 10% drift, two other longitudinal bars buckled on the east side. Failure occurred when a spiral on the west side broke as the column was being pulled to the second cycle at negative 10% drift. Figure 4-1 (A) and (B) show the west side after failure occurred.

##### **4.2.2 Forces and Displacements**

The accumulated lateral force-displacement hysteresis curve for all cycles of RSC is shown in Fig. 4-2 (A). The maximum force, 12.44 kips (55.34 kN) occurred at 1.24 in. (31.50 mm) during the first cycle to negative 3% drift. However, since the clear cover was not symmetrical, the maximum force when the column was cycled in the positive direction was 10.93 kips (48.62 kN), which was recorded at 1.354 in. (34.39 mm) during the first cycle to positive 3% drift. The peak force in the positive direction was lower by 12% due to the lower effective depth of the column for loading in the east direction caused by the thicker concrete cover on the west side of the column.

To eliminate the effect of unequal concrete covers, the average force-displacement envelope was obtained (Fig. 4-3). This envelope was calculated by averaging of the absolute value of the peak displacements in the positive and negative directions for the first cycle at each drift and then averaging the corresponding forces. Figure 4-4 shows both the positive and negative side of the force-displacement envelope. The deeper clear cover on the west side explains the higher forces experienced on the negative side of the envelope. The drop in the negative side envelope forces occurred once the concrete cover on the west side began to spall off. The same drop was not observed in the positive side envelope because the cover was thinner, so once the thicker negative side cover started to spall off, the effect that the unsymmetrical clear cover had on the column response decreased and the capacity of the two sides became closer.

Figure 4-5 shows the absolute measured residual drift ratios versus the maximum drift ratios. The values on this graph are based on data obtained when the column was stopped between cycles at zero load to specifically evaluate residual drift. In order to normalize the positive or negative sign, absolute values were used. RSC experienced a nearly linear relationship between the residual and the maximum drift ratios. A linear regression analysis of the data showed that the residual drift was approximately 81.9% of the maximum drift.

Figure 4-6 shows the idealized force-displacement curves used to estimate the displacement ductility capacity. Displacement ductility is defined as the ratio of the ultimate displacement divided by the effective yield displacement. An elasto-plastic idealization of the force displacement envelope was used to determine the effective yield point. To create this elasto-plastic curve, a line was drawn through the linear portion of the envelope through the point of first yield of a longitudinal bar. It extended up to a horizontal line which was placed to equate the areas above and below the force-displacement plot (equal energy approach). The intersection of these two lines represents the effective yield point. Based on this displacement and using the displacement at failure of the column, the displacement ductility capacity was 7.94.

#### **4.3 RNC**

##### **4.3.1 General Observations**

The concrete cover began to spall off on the east side after the first run to positive 3% drift, and on the west side after the first run to negative 3% drift. After the first push to positive 5% drift, two spirals and one SMA bar were exposed on the west side of the column. One SMA bar became visible on the east side of the column following the first cycle to negative 5% drift, although no spirals could be seen. More spalling occurred in the subsequent runs on both sides of the column, exposing more of the SMAs. Just after the first push to 7% drift it became apparent that the core concrete was starting to experience damage. The crack at the footing column interface was opening wider with each cycle. By the second cycle to positive 7% drift, a total of 7 SMA bars were visible, and the eighth became visible at the footing column interface after the second cycle to positive 10% drift. By the second pull to negative 10% drift the column capacity had dropped by 44.2% relative to the peak, and the column was



considered to have failed. No spirals were broken and there were no signs of the SMA buckling. Figure 4-7 and 4-8 show RNC after testing was complete.

#### 4.3.2 Forces and Displacements

The accumulated lateral force-displacement hysteresis curve for all cycles of RNC is shown in Fig. 4-2 (B). During and after the first cycle at 3% drift, the hysteresis curves were of flag shape indicating that the overall response is controlled by the SMA bars. The flag shape behavior of the SMA results in decreased residual displacement of the column. At 7% drift the flag shape begins to widen, although the loading and unloading plateau are still visible. During the last cycle (10% drift) the force had diminished significantly and the residual drift increased, making the flag-shape response less apparent. The maximum force, 9.37 kips (41.68 kN) occurred at 1.13 in. (28.70 mm) during the first cycle to negative 3% drift.

The average force-displacement envelope is shown in Fig. 4-9 (calculated using the same method as described for RSC). Figure 4-10 shows both the positive and negative side of the force-displacement envelope. There is little difference between the two curves. Specimen RNC experienced rapid force degradation as the test progressed. The definite cause is unknown, though it may relate to the weak bond between the smooth surface of the SMA and conventional concrete. It is widely accepted that failure in a column has occurred once the force drops to 85% of the maximum load<sup>24</sup>. The force dropped below this level after the first cycle to positive 5% drift, and therefore the column could have been considered as failed. However, because no damage was apparent in the spiral or the SMA bars testing continued up to 10% drift.

Figure 4-11 shows the absolute value of residual displacement versus the maximum drift reached. The values on this graph are based on data obtained when the column was stopped between cycles at zero load to specifically evaluate residual drift. Some data was following a positive cycle, while other measurements were taken after a negative cycle; therefore, in order to normalize the positive or negative sign, absolute values were used. This is valid because the significance of residual drift ratio depends on its magnitude regardless of the sign. RNC had very low residual displacement up through 4% drift. At 4% maximum drift the residual drift was only 0.24%. Then from a maximum drift of negative 5% to positive 10% drift the residual displacement steadily increased from 0.61% to 6.34%. Once the column reached 10% drift there was a significant and rapid jump in permanent offset; after the first push to positive 10% drift the residual drift was 2.51% but after the second pull to negative 10% drift (the last run) the residual drift had increased to 6.34%. A linear regression analysis of the data showed that the residual drift was approximately 26.8% of the maximum drift.

Figure 4-12 shows the elasto-plastic idealization curve of the average force-displacement envelope. The method described in Sec. 4.2.2 was used to determine the effective yield point and then to calculate the displacement ductility of 7.60. The ultimate displacement was taken at a point on the envelope where the force capacity dropped to 85% of the peak force.

#### 4.4 RNE

##### 4.4.1 General Observations

Cracking in this column occurred slowly, and most of the cracks were concentrated at the lift interfaces that were created when casting the ECC. These cracks were simply due to the construction method and had little consequence on the column performance. The crack at the footing column interface opened progressively wider with higher drifts (Fig. 4-13). Overall, the cracks within ECC segment were thin, which is typical of ECC behavior since in tension, the fibers prevent widening by holding the material together. No spalling occurred, although slight crushing was visible at the base on the east side after the first push to positive 3% drift. The first SMA bar became visible on the west side between the footing column interface base crack after the second push to positive 5% drift; however, the ECC segment had relatively few cracks and was still fully intact. A spiral was exposed on the east side underneath the base crack after the first pull to negative 7% drift, yet still little damage was observed in the ECC segment.

The ECC did not spall like conventional concrete because the fibers held the cementitious material together. A very small piece of ECC was easily pulled off after the first push to positive 10% drift. After the second push to positive 12% drift the base crack was open wide and it appeared to extend through most of the diameter of the column. At this point small loose dust particles that had accumulated due to the ECC crushing were removed from inside the base crack to investigate the extent of the crack. Up to this point, the crack at the base did not affect the overall performance of the column. The ECC had little damage, especially compared to the conventional concrete, along the column length. In addition to reaching this higher drift ratio, the ECC column capacity was still high. However, the removal of the dust particles from the column base crack may have affected the column performance, because after this point the column forces dropped and the residual displacement increased dramatically. Thus, for comparison purposes, many RNE figures show separately the behavior up to the cycle where the particles were removed (-12% drift) and cycles after this point.

During the first push to positive 14% drift a loud pop sound was heard coming from the west side, although no visible damage had occurred. Then, on the first pull to negative 14% drift another loud pop was heard from the east side, but again no damage could be seen. It was clear from the popping noises and the large drop in load capacity that failure had occurred. Later removal of the SMA rods showed that the popping sounds were from the rupturing of extreme tension SMA bars at the threads just above the couplers embedded in the footing. Figure 4-14 shows RNE after testing was complete.

##### 4.4.2 Forces and Displacements

The accumulated lateral force displacement hysteresis curves for all cycles of RNE up through the second cycle to -12% drift and until the end of testing are shown in Fig. 4-2(C) and (D), respectively. The maximum force, 9.4 kips (41.81 kN) occurred at 1.81 in. (45.97 mm) during the first cycle to positive 4% drift.

The average force displacement envelope through -12% is shown in Fig. 4-15 and all cycles in Fig. 4-16. There is little discrepancy between the positive and negative side curves. The force gradually decreased with increasing drift ratios until reaching 12% drift. After -12% drift, which is when the loose dust particles were removed, the force decreased dramatically. This shows that although these particles were not attached to the column specimen, they appear to have been resisting part of the compression.

Figure 4-17 shows the absolute value of residual drift ratio (regardless of the sign of displacement) versus the maximum measured drift. The values on this graph are based on data obtained when the column was stopped between cycles at zero load to specifically evaluate residual drift. Some data was following a positive cycle, while other measurements were taken after a negative cycle; therefore, in order to normalize the positive or negative sign, absolute values were used. This is valid because the significance of residual drift ratio depends on its magnitude regardless of the sign. RNE had very low residual displacement up to 7% drift. Then from 7% to 12% drift the residual displacement slowly and steadily increased, while still remaining fairly low. Once the column reached -12% drift there was a significant and rapid jump in permanent offset. This radical increase may be attributed to the removal of the small ECC particles from the base crack, and hence is ignored. A linear regression analysis of the data through -12% drift showed that the residual drift was approximately 13.6% of the maximum drift.

An elasto-plastic idealization of the force displacement envelope was used to determine the effective yield point. To create these curves, the average envelopes were used, both up through and after -12 % drift (Fig. 4-18 and 4-19, respectively). The effective yield point was used to find the displacement ductility of 5.53 when considering up through -12% drift, and 6.62 when considering all test data.

## **4.5 Performance Comparison**

### **4.5.1 General Observations**

RNE experienced thin cracks that wrapped around the column at the ECC lift interfaces. These initial cracks did not affect the performance of the ECC; they were simply a result of the method of construction. As the tests progressed, RNE experienced fewer cracks. This phenomenon can be explained by the high tensile strength of ECC and its integrity, since the PVA fibers held the ECC in place and prevented the column from significant cracking.

Spalling occurred in RSC and RNC at the same drift ratio. However, RSC had spalling higher along the column compared to RNC. RNE did not experience spalling, but a type of crushing appeared near the column base. Also, some pieces of ECC delaminated, but the fibers prevented them from detaching, as conventional concrete would have done.

Testing was concluded at the same drift ratio in RSC and RNC. However, using the general rule that failure occurs when the load capacity reaches 85% of the maximum load, then RNC actually failed at 5% drift; which is much lower than RSC drift capacity. RNE sustained higher drifts than the other two columns, with failure

occurring at near 14% drift. Failure mechanisms differed among the three columns. RSC failed when the spiral ruptured and longitudinal bars buckled. RNC failed because of drop in the load capacity. RNE failed when the SMA ruptured at the threads in the bottom coupler. Comparing RSC to RNC shows that the SMA is effective in reducing the damage in the spiral and longitudinal bars. In the case of RNE, the ECC developed fewer cracks along the length of the column, and those that did develop were generally thinner than the cracks on RSC and RNC. Similar to RNC, in RNE there was less damage to the spiral and no buckling occurred in the longitudinal reinforcement.

#### 4.5.2 Residual Drift

Figure 4-20 shows the residual drift versus maximum drift comparison among the three columns, including the linear regression trend lines. Table 4-1 shows the residual drift versus the maximum drift for each column starting at 1% drift. The values in Fig. 4-20 and Table 4-1 are based on the residual drift at zero lateral load following the first push to a positive drift. Comparing the residual drift versus the maximum drift shows that RNE performed much better than both RNC and RSC. A linear regression analysis of the data showed that the residual drift was approximately 13.6% of the maximum drift for RNE through -12% drift, while RNC was nearly two times that at 26.8%, and RSC was about six times higher than RNE at 81.9%. Comparing RNC to RSC shows that the superelastic property of SMA significantly limits residual drift compared to steel. Comparing RNE to RNC shows that the tensile strength of ECC and its unique cracking mechanism successfully reduces residual drift compared to conventional concrete. Overall, the performance of RNE shows that among the three columns the combination of SMA and ECC is the most beneficial to reducing residual drift.

As can be seen from Table 4-1, RSC residual displacement was less than RNC and RNE. At 7% drift, RSC had more residual at this point, whereas in RNC and RNE the residual was hardly noticeable. By the first cycle to positive 10% drift, RSC had the most significant residual. RNC was beginning to have some residual drift at this point; however, the residual drift of RNE was still quite low.

Up through 4% drift, RNC had the lowest residual, but RNE was just above by within 0.1%. From 5% drift and up, RNE had the lowest drift, and RNE withstood higher maximum drifts. This can be attributed to the tensile strength of ECC, and the fact that it experienced less cracking throughout the cycles. This meant that the ECC helped to resist displacement and prevented significant residual deformations. Conversely, the conventional concrete in RNC cracked and spalled and therefore could not aid the column in resisting permanent offset. Both RNC and RNE had lower residual displacement than RSC because of the super-elastic properties of the SMA. One noticeable difference observed in both the SMA-reinforced columns is that residual drift increased at a small rate until failure when the residual drift jumped. On the other hand, RSC residual increased steadily throughout the test.

#### 4.5.3 Forces and Displacements

Figure 4-21 shows the force-displacement envelope comparison and Fig. 4-22 shows the force-drift envelope comparison. As seen in this figure, RSC had the

highest force capacity. Table 4-2 compares the displacement ductility of the three columns, based in the elasto-plastic idealization curves. The initial stiffness of each column was also calculated based on the elasto-plastic idealization curves. RSC had an initial stiffness of 19.2 kip/in. (3.36 kN/mm), which is the highest among the three columns. This can be attributed to the higher modulus of elasticity of steel versus NiTi. RNC and RNE had comparable initial stiffness with 13.1 kip/in. (2.3 kN/mm) and 9.6 (1.7 kN/mm), respectively. The average initial stiffness the SMA columns is approximately 11 kip/in. (1.9 kN/mm), about 36% lower than the conventional steel column. The comparison of the initial stiffness of the SMA columns versus RSC indicates that in the event of an earthquake, the less stiff SMA-reinforced columns would attract less force due to their longer period. Coupled with the displacement recovery of SMA, the lower initial stiffness could be advantageous in earthquakes. RNC and RNE also had comparative peak force; however, RNC experienced rapid force degradation after reaching its maximum value. Comparing RSC to RNC, the degradation in RNC is attributed to the smooth surface of the SMA. There was less bond between the concrete and SMA than with steel. However, if this were the only explanation then similar degradation could be expected in RNE (which was not the case). Therefore, the tensile strength of ECC and the fibers, which held the ECC intact, may have prevented the degradation from occurring in RNE. Comparing the result of RNC and RNE to that of a previous study using SMA and ECC, no further explanation can be found<sup>13</sup>. The specimen in that study showed that combining conventional concrete and SMA (labeled SMAC-1) did not lead to the force degradation seen in RNC. Furthermore, SMAC-1 experienced more distributed damage along the column length in a manner more similar to RSC than RNC. These observations indicate that there may have been something abnormal in the concrete in RNC; however, the result from the concrete cylinder tests and RSC do not show any sign of concrete irregularity. Ultimately, hypotheses can be made, but a definite explanation for the degradation of RNC can not be found without further investigation.

#### 4.5.4 Energy Dissipation

In conventional reinforced concrete, common practice for earthquake design is to yield the steel in order to dissipate energy. Dissipated energy can be quantified by calculating the area under the force displacement envelope. However, with the re-centering capabilities of SMA, the amount of energy dissipation becomes less important as the flag-shaped curve of the hysteresis loop means that the area within the curve is smaller. SMA is a softer material; therefore, the columns will have a longer period and thus, less seismic demand. Still, one impressive property of SMA is the ability to dissipate energy. In order to quantify this point, dissipated energy was calculated for the three columns. The loop area was calculated for every first complete cycle to each drift ratio starting at 1% (but excluding the 1.5% drift cycle). Table 4-3 shows the results. There is more residual displacement in RSC, making the hysteresis curve wider and more energy is dissipated compared to the SMA columns. This points to the benefits of SMA versus steel. Even though less energy was dissipated in the SMA columns, they did not experience as much permanent offset as the conventional column. The two SMA columns dissipated comparable amounts of

energy, though RNE dissipated slightly more than RNC. Additionally, RNE was able to resist more cycles than RNC meaning it could dissipate even more energy.

Figure 4-23 presents the accumulated dissipated energy for the three specimens. One issue of interest here is that the last of several cycles before column failure can dissipate more energy than any other single cycles. This can be seen in the fact that the percentage of the last two runs compared to the total energy dissipation is 66.4% for RSC, 62.5% for RNC. Excluding the last cycle to 14% (because of the removal of particles), the energy dissipation of 10% and 12% drift is 57.6% of the total.

#### 4.5.5 SMA Properties After Column Tests

The superelastic property of the SMAs was an important element in this study. In order to get a better understanding of the material after undergoing the large cyclic loading in the column specimens, the SMA bars were removed from RNC and RNE. Two bars, one from each of the SMA columns, were tested in tension in the same manner as the bar tests before the column test (refer to section 3.4.1). Figure 4-24 and 4-25 show the cyclic response comparison of the two tests performed after the column tests to the one before, and Fig. 4-26 shows the comparison of the stress strain envelopes among the three SMA tests. The bar from RNE was directly next to the extreme tension bar during the column test. This bar showed a lower and less clear yield point, while the stress capacity increased up to the level of the original test by about 25000 microstrains. The bar from RNC was also the bar directly next to the extreme tension bar during the column test. This bar showed a higher yield point, although the curve had also a less defined yield point than the original SMA test. All three SMA tests showed some stress degradation with increasing cycles, although the bar tested from RNC had the highest amount.

The manufacture of the SMA rods was contacted regarding the variability in the stress capacity of the three rods. The conclusion drawn regarding the rounding off of the yield portion of the stress strain curve observed in the two bars tested from the specimens, compared to the fairly sharp transition in the original SMA, is that this indicates that the two rods experienced the effects of cold working from the column cycling. The bar from RNC appears to have experienced some permanent work hardening prior to the tensile test due to the deformations experienced during the cyclic test. The bar from RNE does not seem to show work hardening, though the rounded yield portion indicates that it received sufficient deformation during the column test that it became easier to stress induce the martensite as it approached yield in the tensile test. Some of the difference in the response might be due differences in the temperature at the time of tests, although all the tests were conducted indoors under room temperature that should be nominally the same.

As expected of SMA bars undergoing high strains, there was some residual strain in the bars, though the bar from RNC had a higher percentage. Regardless of slightly variable stress capacity and strain recovery among the three bars, it is important to note that all three exhibited the flag-shape behavior that is typical of SMAs. This shows that even after undergoing large amounts of strain, as the bars removed from RNC and RNE experienced, the SMA still possesses superelastic characteristics. The two bars removed from the columns were tested until failure. Failure occurred in the threads of both of these rods due to stress concentration.



## Chapter 5

### Analytical Studies

#### 5.1 Introduction

Three types of analyses were conducted run for each of the specimens: moment curvature, pushover analysis, and cyclic loading using the computer program OpenSees. This chapter focuses on the aspects relating to the analytical model including the definition and set-up, modeling assumptions, results, and comparison with the experimental results.

#### 5.2 Modeling Method

The computer program “Open System for Earthquake Engineering Simulation” (OpenSees), developed at the University of California, Berkeley, was used in the analytical studies. OpenSees is an object-oriented framework for finite element analysis intended mainly for research purposes. The program includes a large number of elements and offers a great deal of flexibility to the user<sup>25</sup>. Three types of analyses were performed for each column: moment curvature, pushover, and cyclic loading.

The column sections were defined with a fiber model using the measured material properties of the test columns (Fig. 5-1). OpenSees has a variety of pre-defined material models for different applications. All models incorporated the material “concrete01” for both core and cover areas. Concrete01 was suitable for conventional concrete because it assumes no tension capacity (Fig. 5-2). Although ECC was incorporated in RNE to study the contribution of its tensile capacity, this property was not included in the analytical model. This is because ECC-concrete interface was at the top of the footing (the section with the maximum moment) and that the tensile properties were controlled by the weaker of the two materials, which was conventional concrete. Mander’s model was used to calculate the confinement properties for both the conventional concrete and ECC<sup>26</sup>. Although Mander’s Model was developed for conventional concrete, due to a lack of a more specific confinement model for ECC, Mander’s model was assumed to be applicable.

Two types of material models incorporated in OpenSees were selected to model different types of reinforcement. Material models, “steel01” and “uniaxialMaterial Hysteretic”, were tried in the beginning stages of simulation for the reinforcement in all three columns (Fig. 5-3 A and B). Both these materials were developed to model steel, using different parameters for the material definition. Through various trials it was concluded that the “uniaxialMaterial Hysteretic” best modeled the behavior of the steel reinforcement. This material was incorporated into the models for the steel reinforcement in all three columns.

The “uniaxialMaterial Hysteretic” parameters used for the steel are listed in Table 5-1. Three stress and strain points are used to define the steel behavior on the positive and negative sides of the response envelope (eP and sP 1 through 3 and eN and sN 1 through 3, respectively). An additional four factors are defined: “pinchX” and “pinchY” are pinching factors for strain and stress, during re-loading, and “damage1” and “damage2” define degradation of the column response due to ductility and energy, respectively.

By monitoring stresses and strains in the models, it was determined that neither steel01 nor uniaxialMaterial Hysteretic accurately represented the typical flag-shaped response of the SMA bars. Therefore, “pinching4” was selected to model the SMA reinforcement. Pinching4 is capable to model the pinching and degradation of the material and it allows for the definition of multiple points on the material stress strain curve (Fig. 5-4)<sup>25</sup>. The typical flag-shaped behavior with little residual deformation characteristic of NiTi was approximated through the use of the multiple points on the stress strain curve as well as some of the floating point values. The parameters used for NiTi were the same in RNC and RNE columns.

The pinching4 parameters used for NiTi are listed in Table 5-2. The parameters that are not listed in this table were set to zero. Four points on the stress strain curve were defined for both the positive and negative sides and floating points were set as listed in the table. The meanings of the parameters in Table 5-2 are: ePf1 through ePf4 and eNf1 through eNf4 are floating point values that define force (or stress), while ePd1 through ePd4 and eNd1 through eNd4 are floating point values that define displacement (or strain) where P stand for positive and N for negative sides of the response envelopes, respectively. Also, “rDispP(N)” represents the positive (P) and negative (N) side floating point values for the “ratio of the deformation at which reloading occurs to the maximum historic deformation demand.” The parameter “rForceP(N)” represents the positive (P) and negative (N) side floating point values for the “ratio of the force at which reloading begins to force corresponding to the maximum historic deformation demand,” and “uForceP(N)” represents the positive (P) and negative (N) side floating point values for the “ratio of strength developed upon unloading from negative load to the maximum strength developed under monotonic loading” [Ref. 25].

The columns were modeled by assigning elements with appropriate cross sections between nodes. The section properties of the RSC were the same along its length; therefore, two nodes were defined on either end of the column. RNC had different properties at the plastic hinge and the rest of the column; therefore, two elements with different cross section properties had to be defined. The first cross section contained NiTi and the other had steel. These two cross sections were placed between three nodes (node one at the column footing interface, node two at 10 in. (254 mm) above node one representing the length of the NiTi rod above the footing, and node three at the top of the column). RNE was similar to RNC in the NiTi setup, but an additional node was needed at 20 in. (508 mm) above the bottom node for the height of the ECC. All nodes in RSC were connected with “nonlinearbeamcolumn” force based elements which “considers the spread of plasticity along the element”<sup>25</sup>. Nodes in RNC and RNE were connected using the “dispbeamcolumn,” a displacement based element which can be used to model “an element with distributed plasticity with linear curvature distribution”<sup>25</sup>. The use of the different elements in RSC versus RNC and RNE was due to the softness of the SMA, and its recentering characteristics. In the cyclic loading program these properties made it difficult for the “nonlinearbeamcolumn” element connection to convergence when running the analysis, while the dispbeamcolumn prevented errors. Therefore, different elements had to be used in the analyses. Additional parameters that were specific to the type of analysis are discussed in the following sections.

In the OpenSees analysis ultimate points are not explicitly given. Therefore, the failure point in the analysis was assumed to be based on the maximum strain in the core

concrete. Recorders that wrote the data to files were used in order to monitor the stress strain relationship in OpenSees. The ultimate point was taken at the location where the strain dropped below the failure strain (or crushing strain) in the core concrete.

### 5.3 Pushover Analysis

The pushover analysis models were based on incremental displacements of 0.1 in. (2.54 mm) because this increment was small enough to capture the column behavior and allow for response convergence, yet it allowed the analysis to run smoothly since the increment was not too small and did not oversimplified the results, create excess data, or delayed the time of analysis. Initially, it was assumed that there was no P-Delta effect in the columns; however, the test results showed that this effect was not negligible. The test set-up allowed for the P-Delta effects to play a role since the rods that tied the spreader beam on top of the column head to the strong floor went directly to the strong floor. This meant that the axial force was applied at an offset distance relative to the center line of the column-footing interface. Thus the P-Delta effect was employed in both the final pushover and cyclic loading analyses.

#### 5.3.1 RSC

As mentioned in the previous chapter, the clear cover in RSC was not symmetrical. The OpenSees model created a circular section with evenly spaced reinforcement. This means that the clear cover had to be symmetrical. Therefore, in order to represent the actual column geometry in the analytical model, a clear cover of 0.65 in. (16.5 mm) was chosen. As stated in Sec. 4.2.1 the clear cover on the extreme bars on the east side was 0.4 in. (10.2 mm) and on the west side was 0.9 in. (22.9 mm). The average of the two values was 0.65 in. (16.5 mm). The P-Delta effects were activated in this file and the axial load was defined.

A displacement control integrator pattern, used for the pushover, is the command used in OpenSees to determine the relationship of the column response from one time step to the next. During the analysis, various aspects of the response of the model were written to a file using the feature called 'recorders'. Appropriate recorder objects were placed in this file to monitor forces, displacements, and stress and strain in the core concrete. The fact that the strain gages imbedded in the footing of RSC measured strains beyond the yielding of steel indicates that the effect of bond slip influenced the column response. However, this parameter was not successfully accounted for in the analytical models despite many trials. Therefore, the following analytical results neglect bond slip for RSC.

Figure 5-5 shows the analytical pushover curve from OpenSees compared to the measured average force-displacement envelope. Good correlation exists between the measured and analytical curves. The analytical and measured curves agree well with respect to the stiffness, capacity, and the trends in the capacity change in the nonlinear range. At 5% drift ratio the forces in the test data had a percent difference of only 3.0% compared to the analytical model, only 5.8% difference at 7% drift, and 0.8% difference at 10% drift. The measured ultimate drift ratio occurred at 10% while the ultimate analytical drift ratio was 8.44%. This discrepancy is attributed to the fact that the ultimate point in the analytical model was assumed at the initiation of the core damage.

However, in the test some damage to the core penetrated the outer edge before the column was considered to have failed.

Figure 5-6 shows the idealized analytical curves used to find ductility (based on the core concrete crushing strain and the analytical ultimate point). A displacement ductility of 7.85 was found by creating an idealized curve of the pushover analysis in the same manner described in the previous chapter for the test data. The first yield displacement and force were found based on the first appearance of yield strain in the analytical model. The calculated ductility capacity is in excellent agreement with the measured ductility of 7.94.

### 5.3.2 RNC

The OpenSees pushover analysis for RNC was created using similar models as those discussed for RSC. Bond slip was not included in the model for RNC. The coupler acted as a mechanical anchor in the footing, resisting bond slip across the anchorage length because of its flat surface and larger diameter. The strain gage shows that the steel below the couplers did not yield. Since no yielding occurred in that portion, and because of mechanical anchorage effect of the coupler, bond slip could be neglected in the analytical models. Figure 5-7 shows the calculated pushover curve compared to the measured average force-displacement envelope. The initial slope is only slightly steeper in the analytical model compared to the test results. This shows that the model was able to accurately predict the initial force displacement response of the column. In the test, the force dropped rapidly and unexpectedly once the peak force was reached. The rapid force descent in the actual column is possibly due to the slippage of the SMA due to its smooth surface in the plastic hinge region and other possibilities discussed in section 4.5.3. However, the analytical model shows that the force level was maintained up to a displacement of 2 in. (51 mm) followed by a gradual degradation. For this reason, the peak forces estimated by OpenSees are quite a bit higher than the measured data. At 5% drift, the percent difference in the calculated and measured forces was about 22%, at 7% drift the difference was about 24%, and at 10% drift there was nearly a 46% difference. Although these differences are relatively high, they are attributed to the unexpected degradation of the test specimen. The failure point is marked on the analytical curve, which corresponds to the crushing strain at the outer edge of the core concrete. The calculated ultimate force was about 55% higher than the measured result, while the displacement was about 27% lower. The lower ultimate drift of the analytical model can be attributed to the location of core strain measurements, as discussed for RSC.

Figures 5-8 shows the idealized analytical curves used to estimate displacement ductility capacity. The ductility was calculated by creating an idealized curve of the analytical data in the same manner as describe above for RSC. When the calculations are based on the analytical model failure point, the calculated ductility capacity is 5.52. This value is about 27% lower than the measured ductility of 7.60 because forces calculated in the analytical model are quite a bit larger than occurred in the test specimen (and thus the plastic portion of the idealized analytical curve is higher) while the analytical ultimate displacement is lower.

### 5.3.3 RNE

The OpenSees pushover model for RNE was created using similar models as those discussed for RSC. Figure 5-9 shows the analytical pushover curve from OpenSees compared to the measured average force-displacement envelope. Excellent correlation exists between the measured and analytical curve. At 5% drift, the percent difference in the calculate and measured forces was approximately 1.4%, at 7% the difference was 0.3%, and by 10% drift there was less than 2% difference. Before reaching 12% drift, the maximum percent difference in force between the analytical model and the measured results at the same drift ratio was 3.5% or less. This shows that the model is very accurate in predicting forces.

The measured ultimate drift of the test specimen (considering all runs) was approximately 24% higher than the calculated drift. Similar to RSC, the explanation for this discrepancy is that the ultimate point in the analytical model was based solely on the maximum strain in the core concrete at the outside edge. However, in the test the core was able to sustain damage that penetrated in the core before the column failed. At 12% drift, the force in the analytical model is only 3.8% lower than the measured results; this is an excellent correlation.

Figure 5-10 shows the idealized analytical curves used to find ductility based on the analytical failure point (as discussed previously). The calculated ductility capacity was 7.29, which is 14% higher than to the measured ductility. One reason that the ductilities are consistently larger in the analytical model, in addition to the issues mentioned for RSC and RNC, is that the first yield occurred at a lower drift and force than the test specimen, which meant that the analytical elastic slope was steeper.

## 5.4 Cyclic Loading Analysis

OpenSees has the ability to model a user-defined static-cyclic loading pattern. Appropriate recorders were created to monitor forces, displacements, stresses and strains. The peak displacements were defined to match the sequence of drift ratios used during the test as listed in Table 5-3.

### 5.4.1 RSC

The hysteresis curve from the OpenSees analysis is shown superimposed with the measured test curve in Fig. 5-11. Overall, good correlations exist between the two hysteresis curves, both in terms of the force-displacement relationship and residual drifts. Figure 5-12 and Table 5-4 compare the residual drift of the measured data versus the analytical model, both following the first cycle to positive drift. The residual displacement is overestimated by 12.2% at 5% drift and higher for the other drifts. The general trend of the residual drift follows a similar pattern of increasing nearly linearly for both the test data and analytical model. As stated in section 4.2.2, the residual drift was about 82% of the maximum drift, and similarly, the analytical model shows the residual as about 91% of the maximum drift. The forces at the maximum drifts are the same as discussed in the pushover analysis (Section 5.3.1) as the envelope is unchanged in the cyclic analysis. The lack of close agreement in the initial stiffness properties is due to the modeling assumptions for the initial constitutive properties of concrete and bond slip.

#### 5.4.2 RNC

The hysteresis curve from the OpenSees analysis is shown superimposed with the measured test curve in Fig. 5-13. While the correlation is reasonably good for displacements of up to 1.2 in. (30 mm), there are large deviations between the measured and calculated hysteresis curves for larger drift ratios. Figure 5-14 and Table 5-5 compare the measured and calculated residual drifts, both following the first cycle to positive drift. The residual displacement is underestimated by 18.5% at 2% drift and higher for the other drifts. As stated in section 4.3.2, the residual drift was about 26.8% of the maximum drift, while the analytical model shows the residual as only about 9.9% of the maximum drift. The forces at the maximum drifts are the same as discussed in the pushover analysis (Section 5.3.2) as the envelope is unchanged in the cyclic analysis.

#### 5.4.3 RNE

The hysteresis curve from the OpenSees analysis is shown superimposed with the measured test curve in Fig. 5-15. Overall, very good correlation existed between the two hysteresis curves, both in terms of the force-displacement relationship and residual drifts. Figure 5-16 and table 5-6 compare the residual drift of the measured data versus the analytical model, both following the first cycle to positive drift. The residual is underestimated by at least 11% (from 10% drift) with the exception of 12% drift when the analytical model overestimates the residual by about 57%. As stated in section 4.4.2, the residual drift was about 13.6% of the maximum drift, and similarly, the analytical model shows the residual as about 18.2% of the maximum drift. The similarities in forces at the maximum drifts are the same as discussed in the pushover analysis (section 5.3.3) as the envelope is unchanged in the cyclic analysis.

## Chapter 6

### Summary and Conclusions

#### 6.1 Summary

Collapse and severe damage of bridges and buildings during strong earthquakes has been a major concern for structural engineers. Excessive lateral displacement and residual drifts are believed to be one of the major reasons for failure. Column plastic hinges that can dissipate energy without experiencing severe damage and permanent deformation would alleviate these problems. This study focused on developing innovative ductile columns that experience substantially reduced damage and permanent deformation while dissipating the earthquake energy under severe seismic loading. Two innovative materials were incorporated in column plastic hinges: superelastic shape memory alloy (SMA) reinforcement and engineered cementitious composites (ECC).

The primary objective of this study was to investigate the cyclic performance of reinforced concrete columns with SMA longitudinal reinforcement and ECC in the plastic hinge region. The main focus was to evaluate the effectiveness of SMA and ECC in reducing permanent residual column displacements. SMAs are from a unique class of alloys that are able to undergo large levels of strain and still recover their shape. The superelastic property of the SMA NiTi (55.9% Nickel and 44.1% Titanium) in its austenitic phase was investigated in this study. ECC is a fiber-reinforced cement-based composite engineered for high tensile ductility, and high compressive and tensile strength. This study investigated the use of ECC with 2% synthetic poly-vinyl-alcohol (PVA) fiber content by volume.

Three 0.2 scale columns were constructed for cyclic testing in the Large Scale Structures Laboratory of the University of Nevada, Reno. Specimen RSC was made of steel reinforcement and conventional concrete, RNC had SMA reinforcement in the plastic hinge zone and conventional concrete, and RNE had SMA reinforcement and ECC in the plastic hinge zone. The column diameter was 10 in. (254 mm) and the height was 45 in. (1143 mm) in all three specimens. The transverse reinforcement was a spiral formed from #7 gauge galvanized steel wire (0.177 in. (4.5mm) diameter), at 1.5 in. (38.1 mm) pitch. Eight longitudinal bars were incorporated, giving a 2% longitudinal reinforcement ratio in the plastic hinge. RSC consisted of only steel, while RNC and RNE were reinforced with SMA with a length of 14 in. (355.6 mm) in the plastic hinge zone coupled to steel reinforcement. Each specimen was subjected to increasing drifts starting at 0.25% and increasing until column failure.

Following the experimental study, the response of each of the three columns was analyzed with respect to residual drift, force-displacement relationship, moment-curvature relationship, damage progression, plastic hinge length, and energy dissipation. Comparisons were made among the three columns to evaluate the response of the RNC and RNE with respect to the conventional column RSC.

Extensive analytical studies were performed both prior and following the tests. Program OpenSees was used in the analysis. The actual column properties were used in the post-test analyses. Analytical models included moment curvature, pushover force-displacement relationship, and cyclic response of all three specimens. Additional computations were made from the model data to make comparisons among the three specimens with respect to residual drifts, ductility, and energy dissipation. The

calculated and measured results were compared to evaluate the validity of the analytical models.

## 6.2 Conclusions

The following conclusions were made based on the experimental and analytical results:

1. A linear regression analysis of the data showed that the residual drift was approximately 13.6% of the maximum drift for RNE, while in RNC it was 26.8%, and in RSC it was at 81.9%. Comparing RNC to RSC showed that the superelastic property of SMA reduced the residual drift by 67%. Comparing RNE to RNC showed that the tensile strength of ECC and its unique cracking mechanism successfully reduces residual drift by 49%. The combination of SMA and ECC in RNE reduced the residual drift by 83% compared to conventional construction (RSC). Overall, the low residual drift compared to the maximum drift of RNE shows that among the three columns the combination of SMA and ECC is the most beneficial in reducing residual drift.
2. The SMA reinforced columns were superior to the conventional column in limiting residual drift. Both SMA-reinforced columns experienced residual drift that increased at a small rate until failure when the residual drift jumped, whereas RSC residual was significant even at low to moderate drifts. After the first run to positive 10% drift the residual drift was 7.29% for RSC, 2.51% for RNC, and only 1.54% for RNE. Up to 4% maximum drift, no beneficial effect of ECC in reducing residual drift could be noticed because RNC and RNE experienced comparable residual drifts. The advantage of ECC became evident at 5% drift and higher, under which RNE experienced the lowest residual drift.
3. RNE was able to withstand maximum drift ratios of 14% before failure whereas RSC and RNC failed at 10% drift. Additionally, after the first run to 14% drift, RNE only had 4.89% residual drift, which is even lower than what RSC experienced at 10% drift. The higher displacement capacity of RNE is mostly attributed to the tensile strength and cracking behavior of ECC; thus ECC helped to prevent significant residual deformations.
4. The conventional concrete experienced more and wider cracks than the ECC. Spalling did not occur in ECC as it did in conventional concrete. Instead, there was crushing cracks in the ECC, but pieces stayed attached with the PVA fibers. The small crack width of ECC minimizes the need for post-earthquake repair work.
5. The progression of damage shows that RNE would be more serviceable after reaching high drift ratios, indicating that a combination of SMA and ECC is desirable. RSC failed because of longitudinal bar buckling and a ruptured spiral. RNC failed due to decreased load capacity, although neither longitudinal bars buckled nor spirals broke; therefore, the superelastic properties of SMA were helpful in preventing damage to the spiral and longitudinal bars. RNE failed at a very high drift ratio of 14% because of a broken SMA bar at the top of the coupler on the tension side. RNE shows that ECC decreases the amount of damage to the column in both the concrete and the reinforcement because the longitudinal bars did not buckle, the spirals did not break, and there was less concrete damage.



6. The initial stiffness of RSC was 19.2 kip/in. (3.36 kN/mm), and the average initial stiffness the SMA columns was approximately 11 kip/in. (1.9 kN/mm), about 36% lower than RSC. The higher stiffness of RSC is attributed to the higher modulus of elasticity of steel versus NiTi. The comparison of the initial stiffness indicates that in the event of an earthquake, the less stiff SMA-reinforced columns would attract less force due to their longer period. Coupled with the displacement recovery of SMA, the lower initial stiffness could be advantageous in resisting earthquakes.
7. At the second cycle to positive 12% drift, the residual drift of RNE increased dramatically. This is significant because at this cycle the loose particles of ECC were removed from the base crack. Although the particles were not attached, they seem to have been useful in decreasing residual displacement because they still helped resist compression.
8. Pushover and cyclic analytical results using OpenSees showed good correlation with the experimental data. The pushover analysis was able to estimate the force capacity of each column reasonably well. The cyclic analysis response correlated to the general shape of the hysteresis curves, including the flag-shaped response of the SMA columns. In general, residual drifts of the columns were estimated more accurately at higher maximum drifts; however, higher pinching effects of the SMA material model resulted in underestimated residual drifts in RNC and RNE. On the other hand, the analytical model overestimated the residual drift of RSC. The calculated moment curvature relationships using OpenSees did not correlate well with the test data due to simplifying assumptions inherent in the analytical model that do not represent the microscopic behavior of reinforced concrete sections after cracking.



## References

1. Wilson, J.C., and Wesolowsky, M.J., "Shape Memory Alloys for Seismic Response Modification: A State-of-the-Art Review," *EERI Earthquake Spectra*, V. 21, No. 2, May 2005, pp. 569-601.
2. Saadat, S. Salichs, J., Duval, L., Noori, M.N., Hou, Z., Bar-on, I., and Davoodi, H., "Utilization of Shape Memory Alloys for Structural Vibration Control," A summary review for presentation at US-Japan workshop on Smart Materials and New Technologies for Improvement of Seismic Performance of Urban Structures, Disaster Prevention Research Institute Kyoto University, Japan, February 17-18, 1999. Building Research Institute, Tsukuba City, Japan, February 19, 1999.
3. Auricchio, F., Faravelli, L., Magonette, G., Torra, V. (2001) Shape Memory Alloys. Advances in Modelling and Applications. International Center for Numerical Methods in Engineering, Barcelona, Spain, Printed by: Artes Graficas Torres, S.A., Morales 17, 08029 Barcelona, Spain, 2000. pp. 361-392.
4. Ayoub, C., Saiidi, M., and Itani, A., "A Study of Shape-Memory-Alloy-Reinforced Beams and Cubes," , " Center for Civil Engineering Earthquake Research, Department of Civil Engineering, University of Nevada, Reno, Nevada, Report No. CCEER 03-7, October 2003.
5. Saiidi, M., M. Zadeh, C. Ayoub, and A. Itani, "A Pilot Study of Behavior of Concrete Beams Reinforced with Shape Memory Alloys," Journal of Materials in Civil Engineering, ASCE, July 2006, accepted.
6. Ocel, J., DesRoches, R., Leon, R., Hess, G., Krumme, R., Hayes, J., and Sweeney, S., "Steel Beam-Column Connections Using Shape Memory Alloys," *Journal of Structural Engineering*, May 2004 pp. 732-740.
7. El-Tawil, S., and Ortega-Rosales, J., "Prestressed Concrete Using Shape Memory Alloy Tendons" *ACI Structural Journal*, Vol. 101, No. 6, Title No. 101-S84, November-December 2004, pp. 846-851.
8. Desroches, R., McCormick, J., and Delemont, M., "Cyclic Properties of Superelastic Shape Memory Wires and Bars," *Journal of Structural Engineering*, January 2004, pp. 38-46.
9. Li, V., Horii, H., Kabele, P., Kanda, P., and Lim, Y.M., "Repair and Retrofit with Engineered Cementitious Composites," *Engineering Fracture Mechanics* 65 (2000), pp. 317-334.
10. Fischer, G., Li, V., "Effect of Matrix Ductility on Deformation Behavior of Steel-Reinforced ECC Flexural Members under Reversed Cyclic Loading Conditions,"

ACI Structural Journal, Vol. 99, No. 6, Title No. 99-S79, November-December 2002, pp. 781-790.

11. Fischer, G., and Li, V., "Intrinsic Response Control of Moment-Resisting Frames Utilizing Advanced Composite Materials and Structural Elements," ACI Structural Journal, Vol. 100, No. 2, Title No. 100-S18, March-April 2003, pp. 166-176.
12. Fischer, G., Li, V., "Deformation Behavior of Fiber-Reinforced Polymer Reinforced Engineered Cementitious Composite (ECC) Flexural Members under Reversed Cyclic Loading Conditions," ACI Structural Journal, Vol. 100, No. 1, Title No. 100-S4, January-February 2003, pp. 25-35.
13. Wang, H. and Saiidi, M., "A Study of RC Columns with Shape Memory Alloy and Engineered Cementitious Composites," Center for Civil Engineering Earthquake Research, Department of Civil Engineering, University of Nevada, Reno, Nevada, Report No. CCEER 05-1, January 2005.
14. Saiidi, M., and H. Wang, "An Exploratory Study of Seismic Response of Concrete Columns with Shape Memory Alloys Reinforcement," American Concrete Institute, ACI Structural Journal, Vol. 103, No. 3, May-June 2006, pp. 436-443.
15. O'Brien, M., Saiidi, M., and Sadrossadat-Zadeh, M., "A Study of Concrete Bridge Columns Using Innovative Materials Subjected to Cyclic Loading," Center for Civil Engineering Earthquake Research, Department of Civil Engineering, University of Nevada, Reno, Nevada, Report No. CCEER 07-1, January 2007.
16. DesRoches, R., Smith, B., "Shape Memory Alloys in Seismic Resistant Design and Retrofit: A Critical Review of the State of the Art, Potential, and Limitations," Georgia Institute of Technology, School of Civil and Environmental Engineering, Atlanta, GA, April 2003.
17. Otsuka, K. and Wayman, C.M., "Shape Memory Materials," Cambridge University Press. 1999.
18. Dolce, M., Cardone, D., "Mechanical Behaviour of shape memory alloys for seismic applications (2) Austinite NiTi Wires Subjected to Tension," *International Journal of Mechanical Sciences*, V. 43, 2001, pp. 2657-2677.
19. Li, V. C., "Engineered Cementitious Composites," Proceedings of ConMat'05, Vancouver, Canada, August 22-24, 2005, [http://www.engineeredcomposites.com/publications/Conmat05/Li\(ECC\).pdf](http://www.engineeredcomposites.com/publications/Conmat05/Li(ECC).pdf), retrieved November 6, 2005.

20. Li, V.C., and M. Lepech, "General Design Assumptions for Engineered Cementitious Composites," Proceedings of Int'l workshop on HPFRCC in structural applications, Honolulu, Hawaii, USA, May 23-26, 2005, retrieved from <http://www.engineeredcomposites.com/html/publication.html>, November 6, 2005.
21. Li, V., "On Engineered Cementitious Composites (ECC), A Review of the Material and its Applications," *Journal of Advanced Concrete Technology*, Vol. 1 No. 3, November 2003, pp. 215-230.
22. Friedland, I., Mayes, R., et. al., "Recommended LRFD Guidelines for the Seismic Design of Highway Bridges," MCEER Highway Project, Project 094, Task F3-1, State University of New York at Buffalo, November 2001, section 8.8.2, section c8.8.2.5-2.
23. Paulay, T., and Priestley, M.J.N. 1992. Seismic Design of Reinforced Concrete and Masonry Buildings," John Wiley & Sons, Inc., New York.
24. Mortensen, J. and Saiidi, M., "A Performance-Based Design Method for Confinement in Circular Columns," Civil Engineering Department, University of Nevada, Reno, Report No. CCEER 02-7, November 2002.
25. Mazzoni, S., McKenna, F., Fenves, G., et al., "Open System for Earthquake Engineering Simulation User Manual version 1.6.2," Pacific Earthquake Engineering Center, University of California, Berkeley.  
(<http://opensees.berkeley.edu/OpenSees/manuals/usermanual/>)
26. Mander, J.B., Priestley, M.J.N., and Park, R., "Theoretical stress Strain Curve for Confined Concrete Column," *ASCE Journal of Structural Engineering*, V. 114, No. 8, August 1988. pp. 1804-1826.



Table 3-1: Measured Reinforcement Properties

Reinforcement	Yield Stress, ksi (MPa)	Ultimate Strength, ksi (MPa)
<b>SMA</b>	55 (379.2)	***
<b>Steel #4</b>	68.5 (472.3)	111.5 (768.8)
<b>Steel #5</b>	65.6 (452.3)	104.5 (720.5)
<b>Spiral</b>	61.6 (424.7)	73.6 (507.5)

Table 3-2: Measured Concrete and ECC Compressive Strength

Concrete Location	Test Sample	Compressive Strength, ksi (MPa)				
		7-day	28-day	RSC Test Day	RNC Test Day	RNE Test Day
Footing	1	3.180 (21.9)	5.039 (34.7)	5.843 (40.3)	6.093 (42.0)	5.435 (37.5)
	2	3.235 (22.3)	5.207 (35.9)	6.058 (41.8)	5.941 (41.0)	6.289 (43.4)
	3	3.136 (21.6)	5.316 (36.7)	5.993 (41.3)	6.264 (43.2)	6.133 (42.3)
	Average	3.183 (21.9)	5.187 (35.8)	5.965 (41.1)	6.100 (42.1)	5.952 (41.0)
Column & Head	1	3.924 (27.1) *	5.187 (35.8)	6.127 (42.2)	5.865 (40.4)	5.055 (34.9)
	2	3.762 (25.9)	5.232 (36.1)	6.002 (41.4)	5.473 (37.7)	5.225 (36.0)
	3	3.721 (25.7) *	5.231 (36.1)	5.381 (37.1)	4.786 (33.0)	5.661 (39.0)
	Average	3.802 (26.2)	5.217 (36.0)	5.837 (40.2)	5.669 (39.1)	5.314 (36.6)
ECC	1	1.703 (11.7)	4.717 (32.5)	-	-	5.031 (34.7)
	2	2.235 (15.4)	4.792 (33.0)	-	-	5.130 (35.4)
	3	1.650 (11.4)	4.727 (32.6)	-	-	4.835 (33.3)
	4	-	-	-	-	5.765 (39.7)
	Average	1.863 (12.8)	4.746 (32.7)	-	-	5.191 (35.8)

Table 3-3 ECC Mix Design

	Cement	Fly Ash	Sand	Fiber	Super-plasticizer	HPMC	Total per pail*	Total all pails
Weight (lbs)	15	14.2	14.6	0.6	0.06	0.03	44.5	133.5
Percent of Total by Weight (%)	33.72	31.92	32.82	1.35	0.13	0.07	100.0	

Table 3-4: Actual Load Cycle

Cycle Number	Drift Reached		
	RSC	RNC	RNE
1	0.27	0.27	0.27
2	0.06	-0.25	-0.24
3	-0.24	0.53	0.52
4	0.03	-0.50	-0.49
5	0.52	0.53	0.53
6	0.08	-0.49	-0.49
7	-0.49	1.04	1.03
8	0.53	-1.00	-1.00
9	-0.49	1.03	1.03
10	1.02	-1.00	-1.00
11	-0.99	1.54	1.53
12	1.02	-1.50	-1.51
13	-0.99	1.54	1.54
14	1.52	-1.51	-1.51
15	-1.49	2.04	2.04
16	1.52	-2.01	-2.01
17	-1.49	2.04	2.04
18	2.02	-2.01	-2.00
19	-1.99	3.04	3.04
20	2.02	0.17	0.25
21	-1.99	-3.00	-3.00
22	3.03	3.04	3.04
23	0.96	-3.01	-3.01
24	-2.99	4.04	4.04
25	3.03	0.24	0.20
26	-2.99	-4.00	-4.00
27	4.03	4.04	4.04
28	1.79	-4.00	-4.01
29	-3.99	-0.25	5.04
30	-2.02	5.03	0.37
31	4.03	-5.00	-5.01
32	-4.00	5.04	5.04
33	5.03	-5.00	-5.00
34	2.66	-0.61	7.04
35	-5.00	7.04	0.48
36	-2.94	1.36	-7.01
37	5.03	-7.01	7.04
38	-4.42	7.04	-7.01
39	-2.92	-7.00	-0.39
40	7.03	10.04	10.03
41	4.40	2.51	1.56
42	-7.00	-10.00	-10.00
43	-4.87	10.04	10.04
44	7.03	-10.00	-10.00
45	-7.00	-6.34	12.04
46	10.03		1.43
47	7.24		-12.01
48	-9.99		12.04
49	-7.80		-12.01
50	10.03		14.04
51	-9.99		4.86
52	8.51		-13.76
53			-9.06



Table 4-1: Residual versus Maximum Drift

Maximum			Residual								
			RSC			RNC			RNE		
			Displacement		Drift	Displacement		Drift	Displacement		Drift
(in)	(mm)	(in)	(mm)	(in)		(mm)	(in)		(mm)		
0.45	11.4	1	0.06	1.44	0.13	0.04	1.10	0.10	0.05	1.15	0.10
0.675	17.1	1.5	0.08	1.9	0.17	0.05	1.1	0.10	0.05	1.4	0.12
0.9	22.9	2	0.14	3.7	0.32	0.04	1.1	0.10	0.07	1.8	0.15
1.35	34.3	3	0.44	11.1	0.97	0.07	1.7	0.15	0.11	2.9	0.25
1.8	45.7	4	0.80	20.4	1.79	0.11	2.8	0.25	0.13	3.2	0.28
2.25	57.2	5	1.20	30.4	2.66	0.16	4.2	0.36	0.16	4.0	0.35
3.15	80.0	7	2.00	50.8	4.44	0.61	15.6	1.37	0.23	5.8	0.51
4.5	114.3	10	3.28	83.4	7.29	1.13	28.7	2.51	0.69	17.6	1.54
5.4	137.2	12							0.64		1.43
6.3	160.0	14							2.20		4.89

Table 4-2: Displacement Ductility Comparison

	Displacement				
	Effective Yield Displacement		Ultimate Displacement		Displacement Ductility
	inches	mm	inches	mm	
RSC	0.57	14.4	4.50	114.4	7.94
RNC	0.59	15.1	4.51	114.5	7.60
RNE Through -12%	0.98	24.9	5.41	137.4	5.53
RNE All Cycles	0.95	24.0	6.25	158.9	6.62

Table 4-3: Energy Dissipation Comparison

		Drift Ratio							
		1%	2%	3%	4%	5%	7%	10%	12%
RSC	Kip-in	1.4	5.7	15.3	24.3	34.0	59.3	100.1	---
	kN-mm	160.4	640.6	1724.2	2747.8	3837.0	6700.0	11309.8	---
RNC	Kip-in	1.19	2.96	7.65	12.1	16.12	30.77	39.24	---
	kN-mm	134.5	334.4	864.3	1367.1	1821.3	3476.5	4433.5	---
RNE	Kip-in	1.26	3.27	7.9	11.53	21.19	29.91	48.82	53.28
	kN-mm	142.4	369.5	892.6	1302.7	2394.2	3379.4	5515.9	6019.8

Table 5-1: “UniaxialMaterial Hysteretic” Parameters for Steel Reinforcement

A) #4 Rebar, B) #5 Rebar

A)			B)		
	Label	Value		Label	Value
Positive Side	s1p	68.5	Positive Side	s1p	65.6
	e1p	0.00236		e1p	0.00258
	s2p	70.39		s2p	66.04
	e2p	0.0061		e2p	0.0079
	s3p	111.5		s3p	104.5
	e3p	0.095		e3p	0.103
Negative Side	s1n	-68.5	Negative Side	s1n	-65.6
	e1n	-0.00236		e1n	-0.00258
	s2n	-70.39		s2n	-66.04
	e2n	-0.0061		e2n	-0.0079
	s3n	-111.5		s3n	-104.5
	e3n	-0.095		e3n	-0.103
Miscellaneous	pinchX	0	Miscellaneous	pinchX	0
	pinchY	1		pinchY	1
	damage1	0		damage1	0
	damage2	-1		damage2	-1
	beta	0		beta	0

Table 5-2: “Pinching4” Parameters For SMA Reinforcement

	Label	Value
Positive Side	ePf1	55
	ePd1	0.006
	ePf2	66.9707
	ePd2	0.04
	ePf3	120
	ePd3	0.2
	ePf4	100
	ePd4	0.3
	rDispP	-0.09
	rForceP	0.25
	uForceP	-0.2
Negative Side	eNf1	-55
	eNd1	-0.006
	eNf2	-66.9707
	eNd2	-0.04
	eNf3	-120
	eNd3	-0.2
	eNf4	-100
	eNd4	-0.3
	rDispN	-0.09
	rForceN	0.25
	uForceN	-0.2
Miscellaneous	gE	10
	dmgType	energy

Table 5-3: Peak Displacement Points Used for Cyclic Analysis

	Displacement		Drift
	inches	mm	%
All Three Columns	0.1125	2.9	0.25
	0.225	5.7	0.5
	0.45	11.4	1
	0.675	17.1	1.5
	0.9	22.9	2
	1.35	34.3	3
	1.8	45.7	4
	2.25	57.2	5
	3.15	80.0	7
Only RNE	4.5	114.3	10
	5.4	137.2	12
	6.3	160.0	14

Table 5-4: RSC Residual Displacement: Measured vs. Calculated

Max Drift Reached	Measured			Calculated			Percent Difference (Measured vs. Calculated)
	Residual Displacement	Residual Drift		Residual Displacement	Residual Drift		
%	inches	mm	%	inches	mm	%	%
1	0.06	1.4	0.13	0.04	1.1	0.09	24.9
1.5	0.08	1.9	0.17	0.14	3.6	0.32	87.9
2	0.14	3.7	0.32	0.28	7.1	0.62	94.0
3	0.44	11.1	0.97	0.60	15.2	1.33	37.5
4	0.80	20.4	1.79	0.95	24.0	2.10	17.6
5	1.20	30.4	2.66	1.34	34.1	2.98	12.2
7	2.00	50.8	4.44	2.28	58.0	5.07	14.2
10	3.28	83.4	7.29	3.72	94.5	8.27	13.4

Table 5-5: RNC Residual Displacement: Measured vs. Calculated

Max Drift Reached	Measured			Calculated			Percent Difference (Measured vs. Calculated)
	Residual Displacement	Residual Drift		Residual Displacement	Residual Drift		
%	inches	mm	%	inches	mm	%	%
1	0.04	1.1	0.10	0.01	0.4	0.03	66.6
1.5	0.05	1.1	0.10	0.04	0.9	0.08	20.7
2	0.04	1.1	0.10	0.04	0.9	0.08	18.5
3	0.07	1.7	0.15	0.01	0.4	0.03	77.5
4	0.11	2.8	0.25	0.02	0.5	0.04	83.2
5	0.16	4.2	0.36	0.01	0.3	0.03	91.7
7	0.61	15.6	1.37	0.09	2.3	0.20	85.1
10	1.13	28.7	2.51	0.50	12.8	1.12	55.5

Table 5-6: RNE Residual Displacement: Measured vs. Calculated

Max Drift Reached	Measured			Calculated			Percent Difference (Measured vs. Calculated)
	Residual Displacement	Residual Drift		Residual Displacement	Residual Drift		
%	inches	mm	%	inches	mm	%	%
1	0.05	1.2	0.101	0.02	0.4	0.036	64.0
1.5	0.05	1.4	0.121	0.03	0.8	0.067	44.3
2	0.07	1.8	0.155	0.05	1.3	0.114	26.3
3	0.11	2.9	0.253	0.06	1.5	0.129	49.0
4	0.13	3.2	0.278	0.06	1.5	0.135	51.4
5	0.16	4.0	0.354	0.06	1.6	0.137	61.4
7	0.23	5.8	0.506	0.17	4.3	0.372	26.5
10	0.69	17.6	1.544	0.62	15.7	1.371	11.2
12	0.64	16.3	1.430	1.01	25.6	2.239	56.6
14	2.20	55.9	4.890	1.47	37.3	3.261	33.3

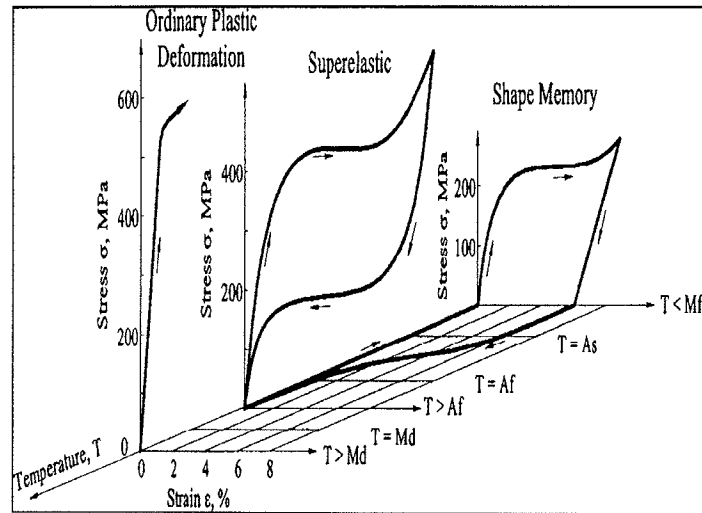


Figure 2-1: Typical Three-Dimensional Stress Strain Temperature Diagram of SMA<sup>8</sup>

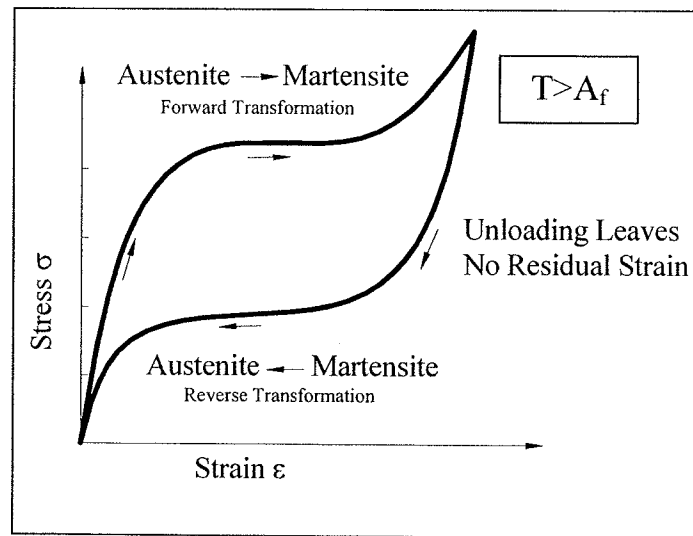


Figure 2-2: Superelastic Effect Idealized Stress Strain Curve<sup>16</sup>

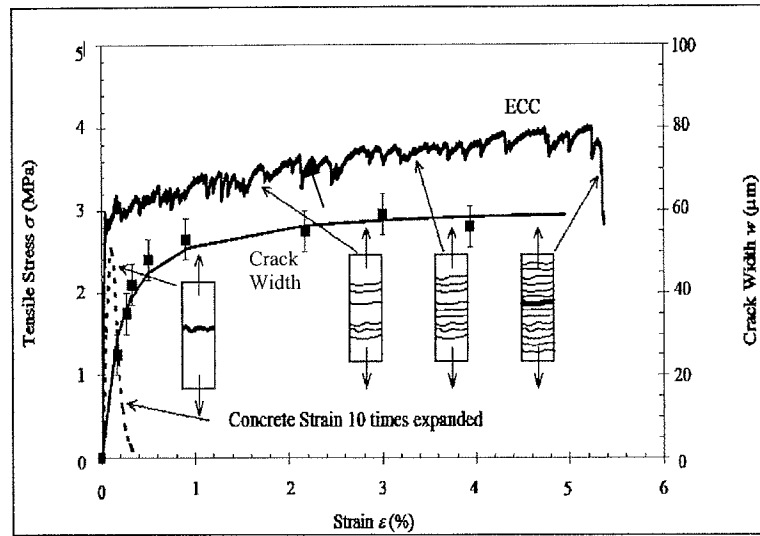


Figure 2-3: Typical Tensile Stress-Strain Curve and Crack Width Development of ECC<sup>19</sup>

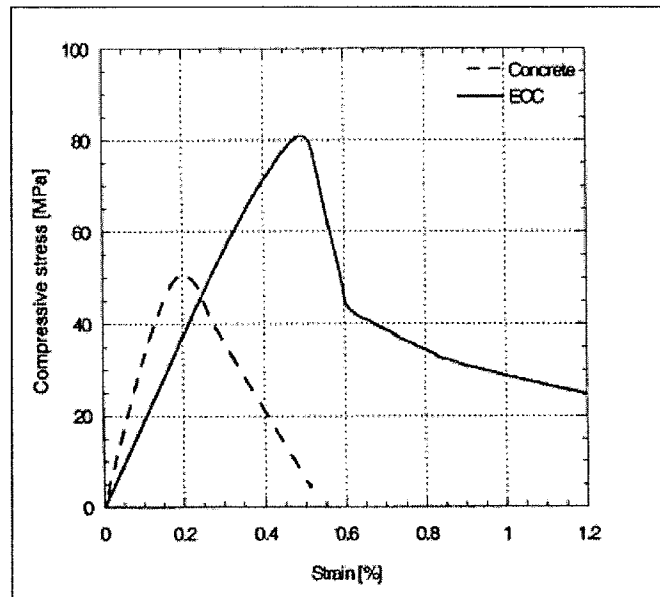


Figure 2-4: Typical Compressive Stress-Strain Behavior of ECC and Concrete<sup>12</sup>

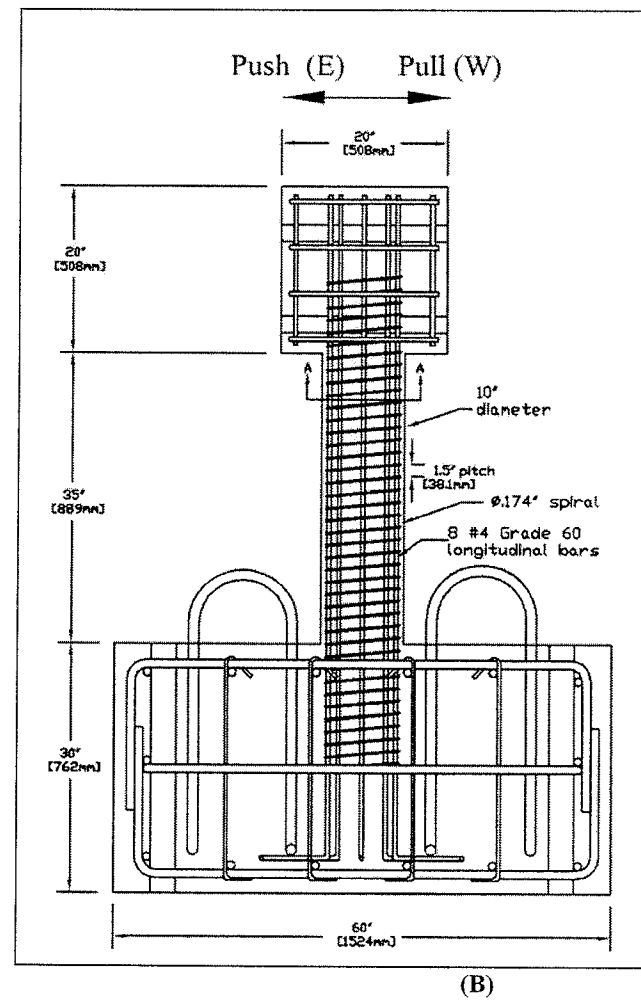
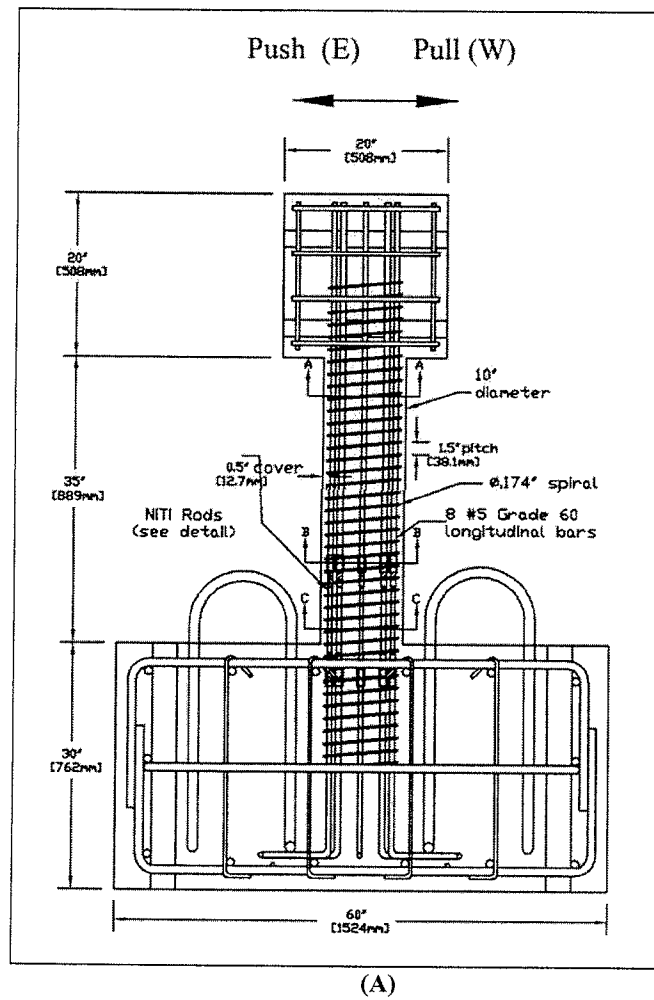


Figure 3-1: Column Details: A) RNC and RNE, B) RSC

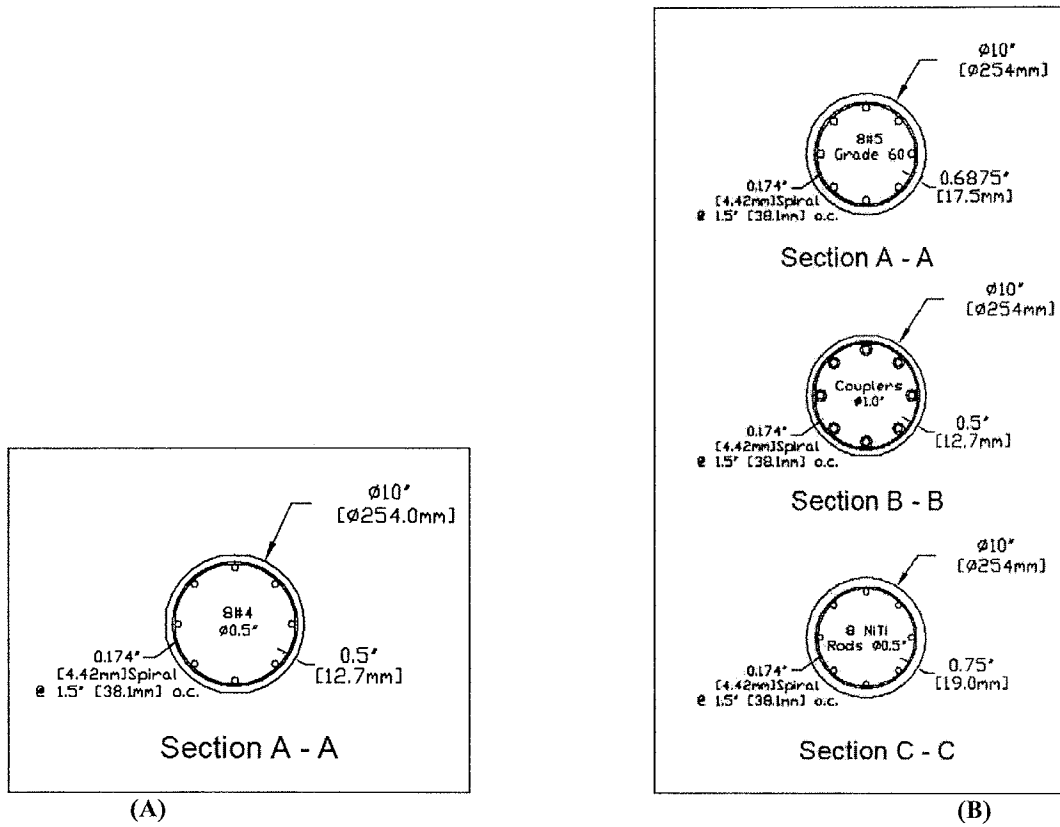


Figure 3-2: Cross Sections A) RSC, B) RNC and RNE

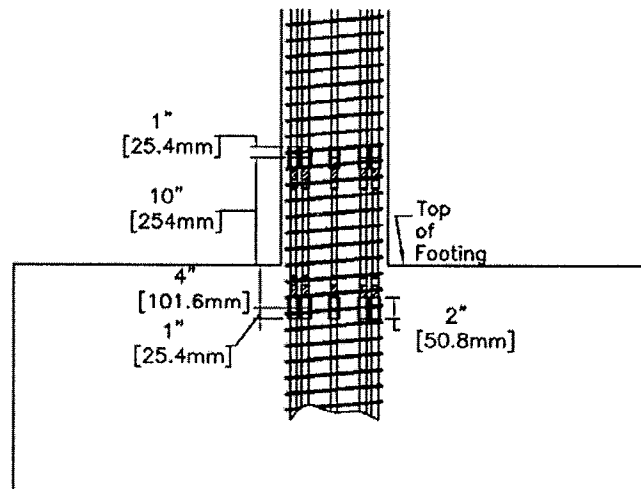


Figure 3-3: Plastic Hinge Detail

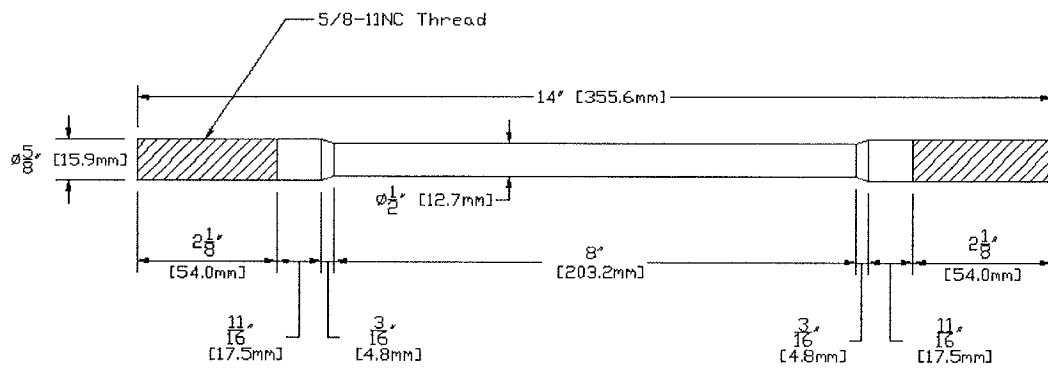


Figure 3-4: NiTi Rod Detail

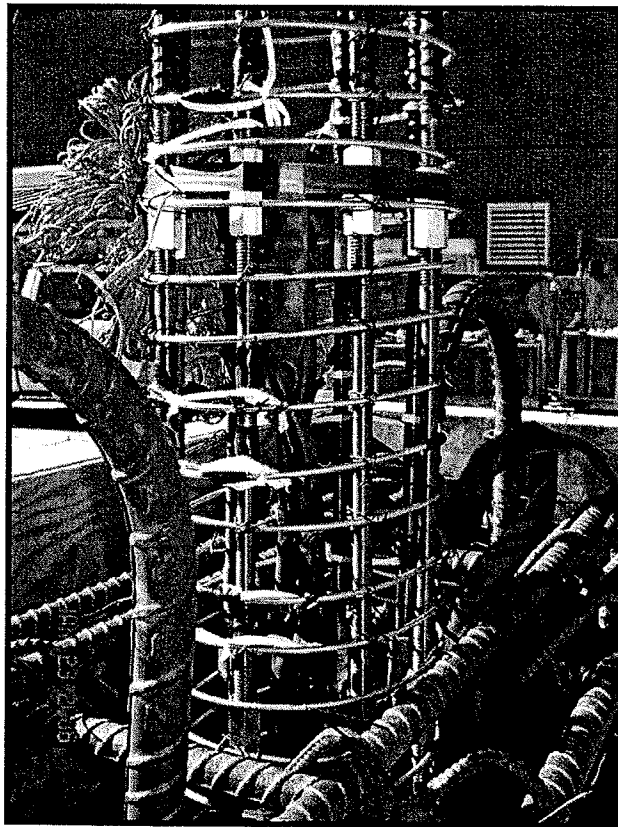


Figure 3-5: Steel-NiTi Connection RNC, RNE



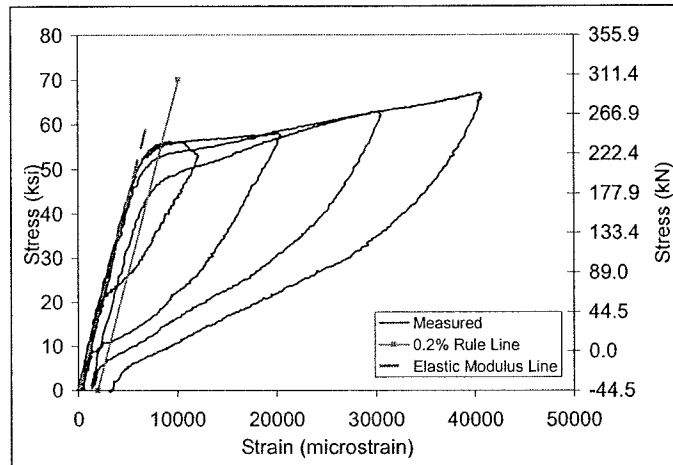


Figure 3-6: NiTi Stress Strain Graph from Laser Transducer

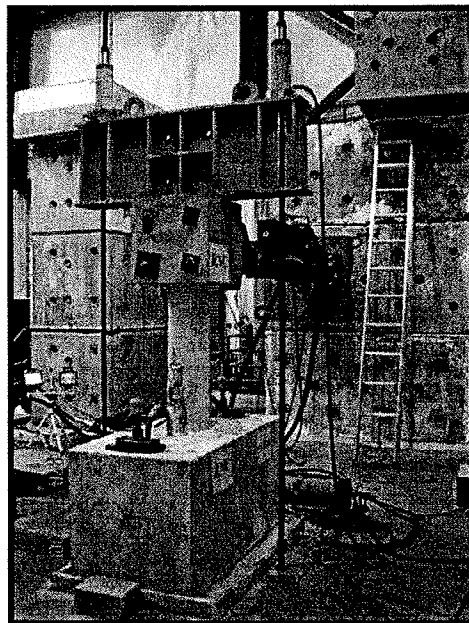


Figure 3-7: RNC Test Setup

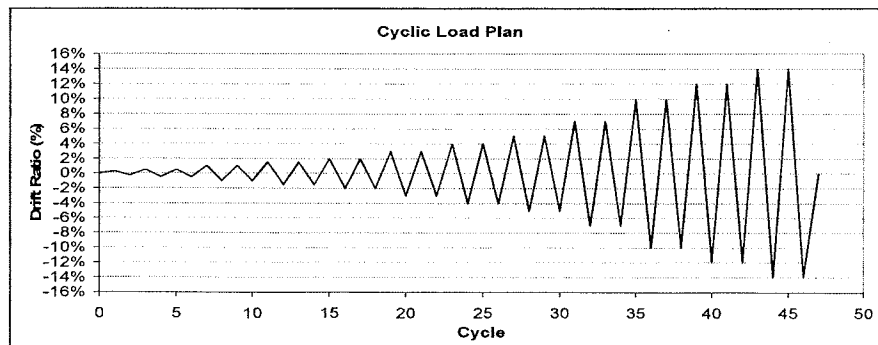
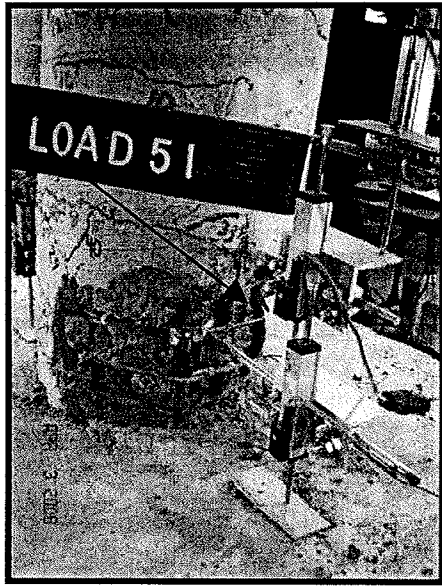
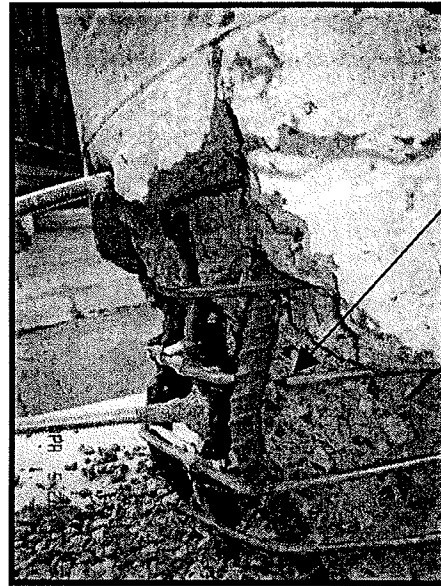


Figure 3-8: Cyclic Load Plan

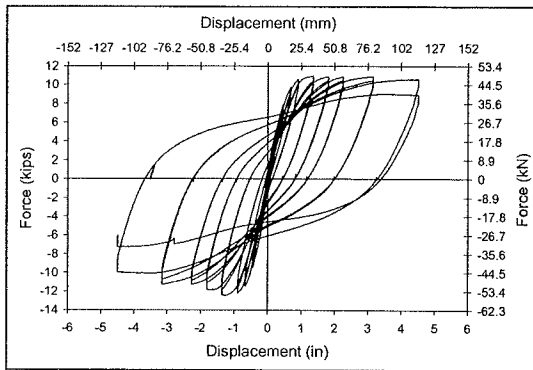


(A)

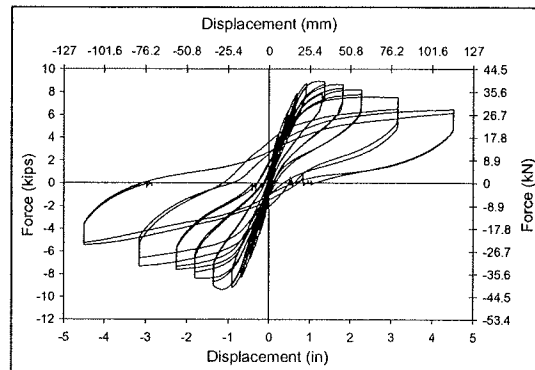


(B)

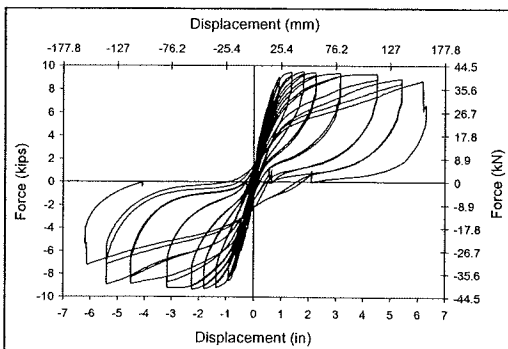
Figure 4-1: A) and B) RSC Spiral Rupture on West Side after Second Cycle to -10% Drift



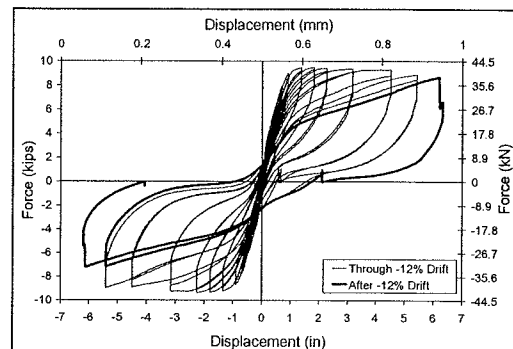
A



B



C



D

Figure 4-2: Force Displacement Hysteresis A) RSC, B) RNC, C) RNE, D) RNE Before and After -12% Drift

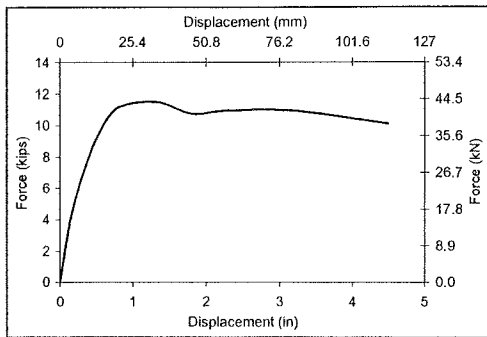


Figure 4-3: RSC Average Force Displacement Envelope

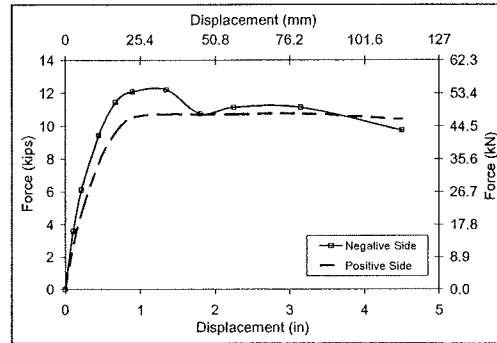


Figure 4-4: RSC Positive and Negative Force Displacement Envelopes

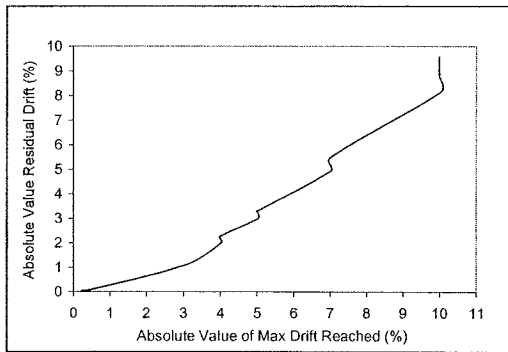


Figure 4-5: RSC Residual Displacement vs. Maximum Drift

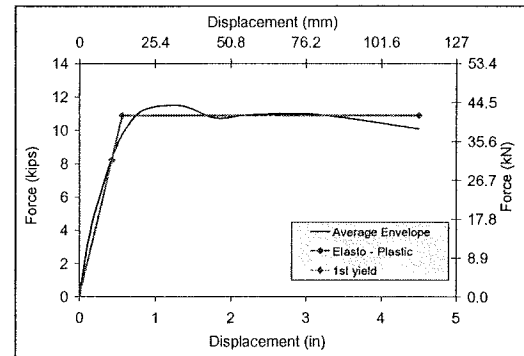


Figure 4-6: RSC Idealized Force-Displacement Envelope

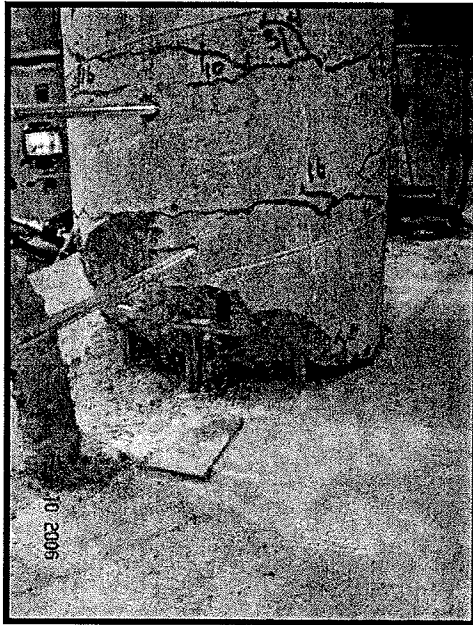


Figure 4-7: RNC North Side After Testing

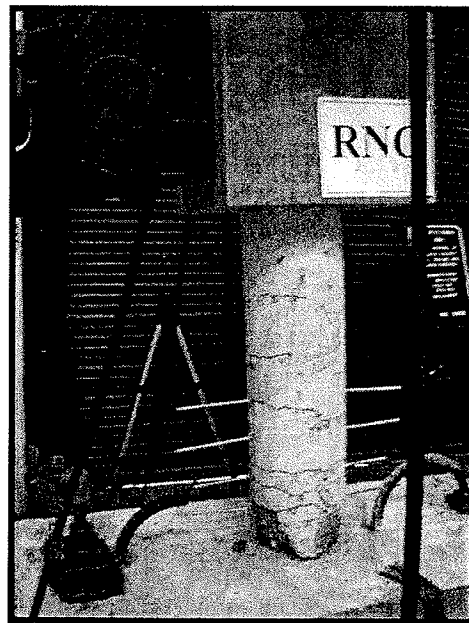


Figure 4-8: RNC Permanent Offset After Testing

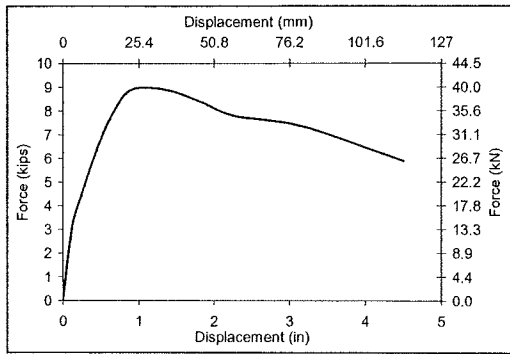


Figure 4-9: RNC Average Force Displacement Envelope

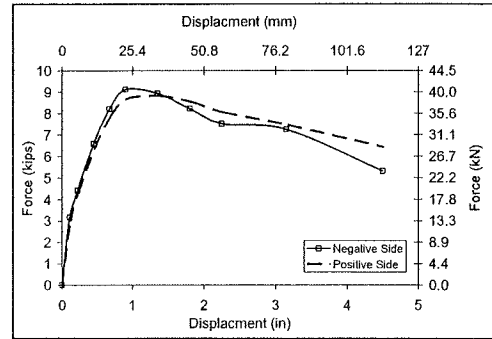


Figure 4-10: RNC Positive and Negative Force Displacement Envelopes

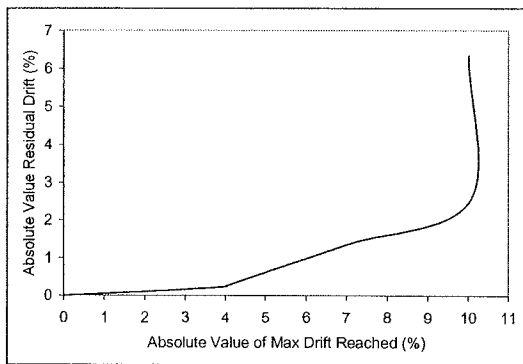


Figure 4-11: RNC Residual Displacement vs. Maximum Drift

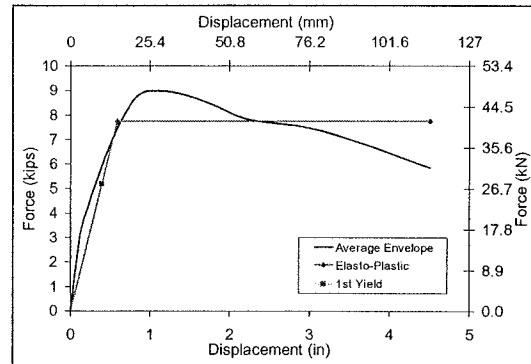


Figure 4-12: RNC Idealized Force-Displacement Envelope



Figure 4-13: RNE Development of Base Crack

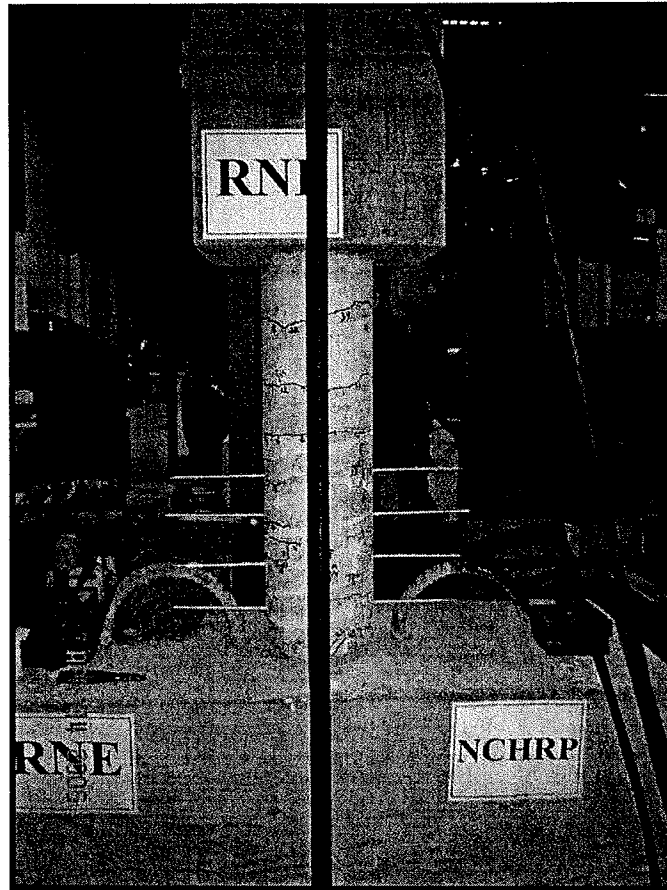


Figure 4-14: RNE Permanent Offset After Testing

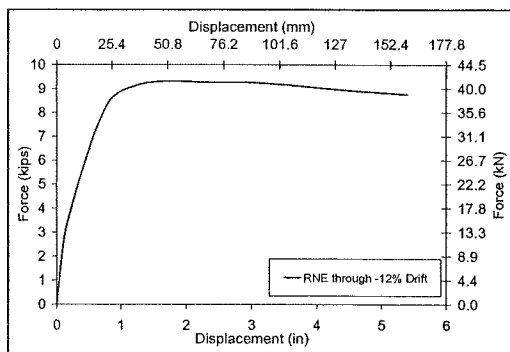


Figure 4-15: RNE Average Force Displacement

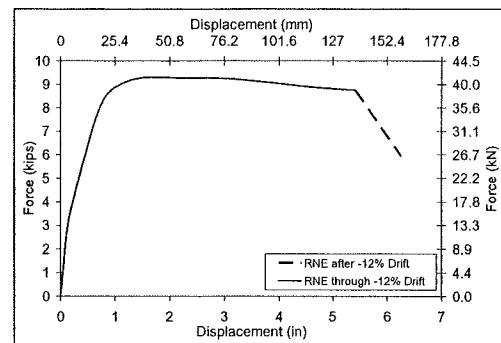


Figure 4-16: RNE Force Displacement Envelope to End of Test

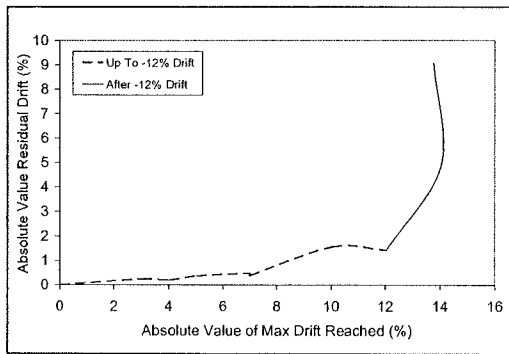


Figure 4-17: RNE Residual Displacement vs. Maximum Drift

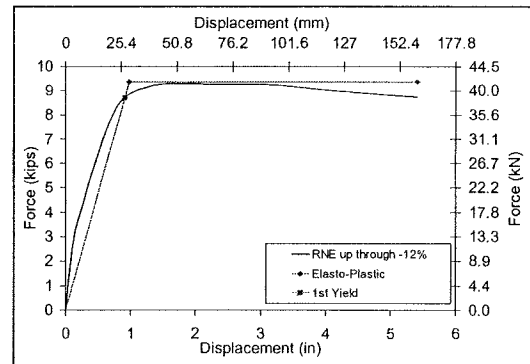


Figure 4-18: RNE Idealized Force-Displacement Envelope through -12%

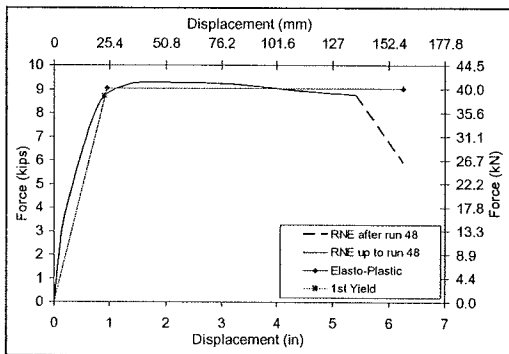


Figure 4-19: RNE Idealized Force-Displacement Envelope to End of Test

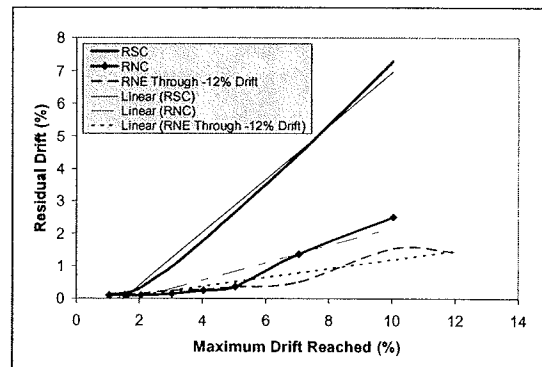


Figure 4-20: Residual Drift vs. Maximum Drift Comparison

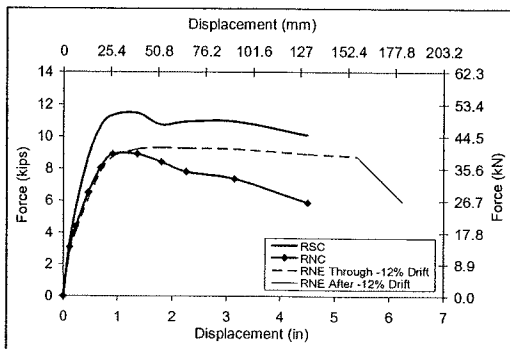


Figure 4-21: Force vs. Displacement Envelope Comparison

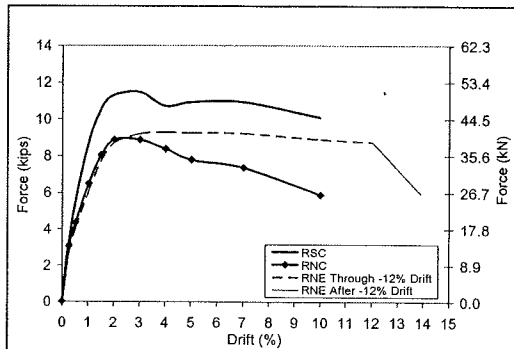


Figure 4-22: Force vs. Drift Envelope Comparison

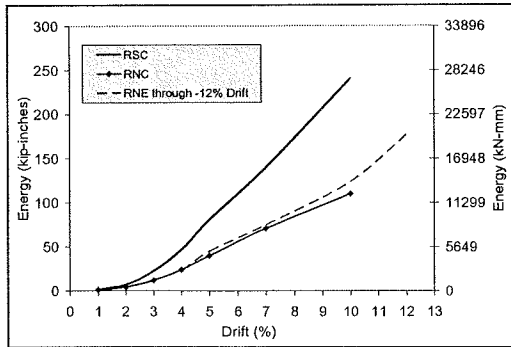


Figure 4-23: Accumulated Energy Dissipation Comparison

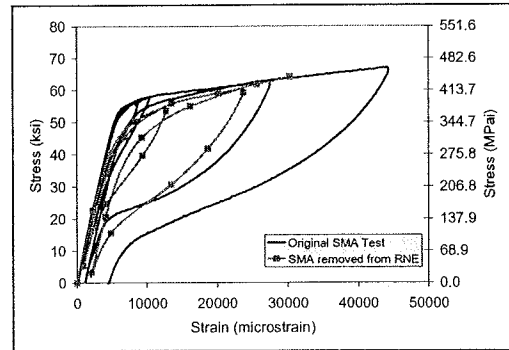


Figure 4-24: Comparison of SMA Tensile Tests Original vs. RNE Bar

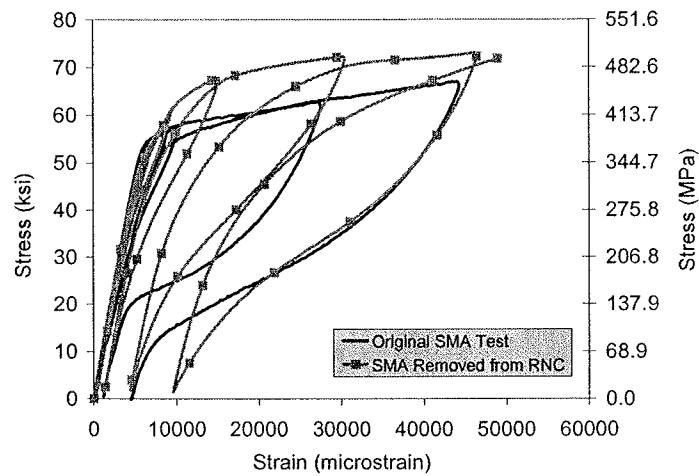


Figure 4-25: Comparison of SMA Tensile Tests Original vs. RNC Bar

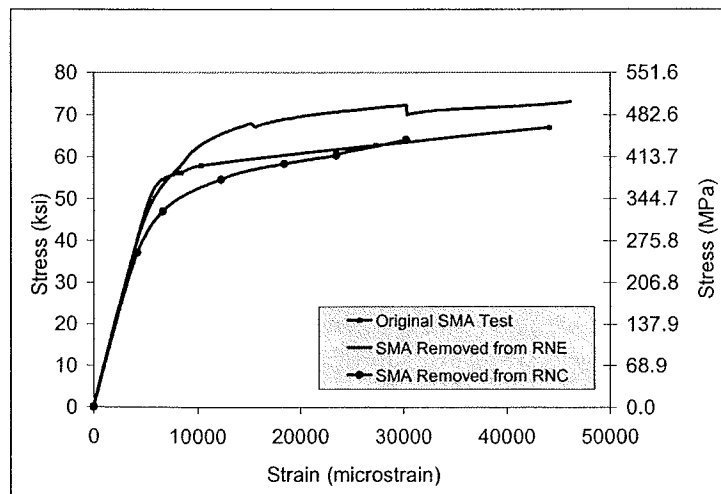


Figure 4-26: SMA Tensile Tests Envelope Before and After Column Tests

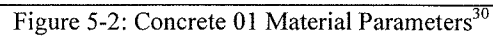
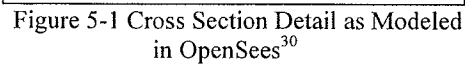
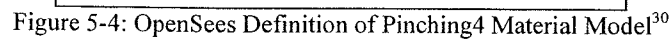


Figure 5-3: Steel Material Models: A) Steel 01 B) UniaxialMaterial Hysteretic<sup>30</sup>





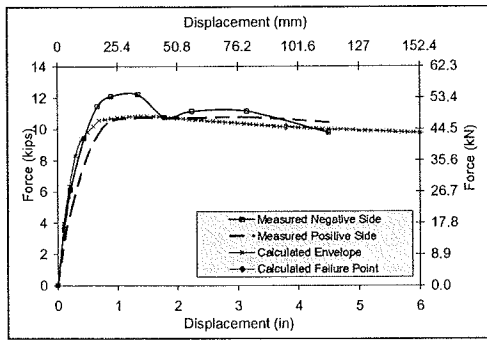


Figure 5-5: RSC OpenSees Analysis vs Measured Average Envelope

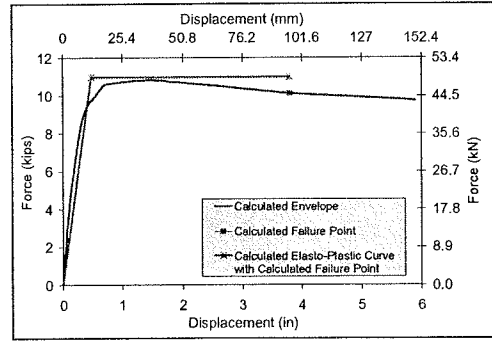


Figure 5-6: RSC Idealized Calculated Curves

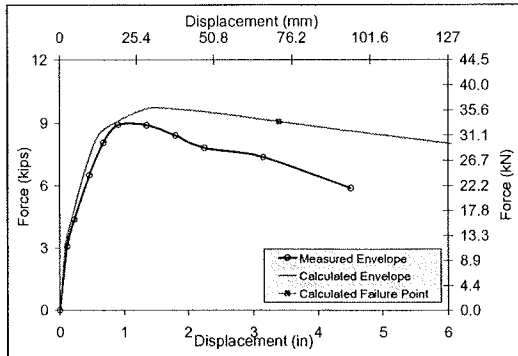


Figure 5-7: RNC Pushover Measured vs. Calculated

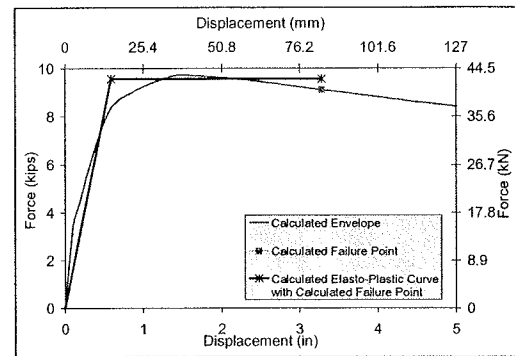


Figure 5-8: RNC Idealized Calculated Curves

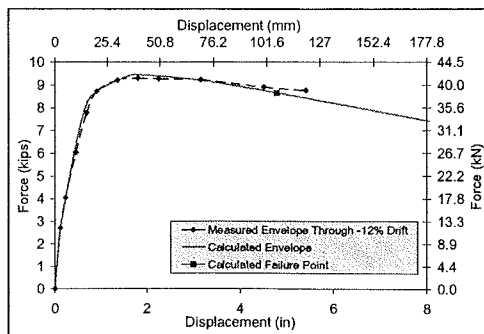


Figure 5-9: RNE Pushover Measured vs. Calculated

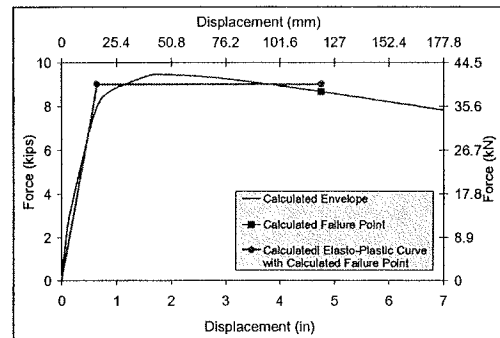


Figure 5-10: RNE Idealized Calculated Curve

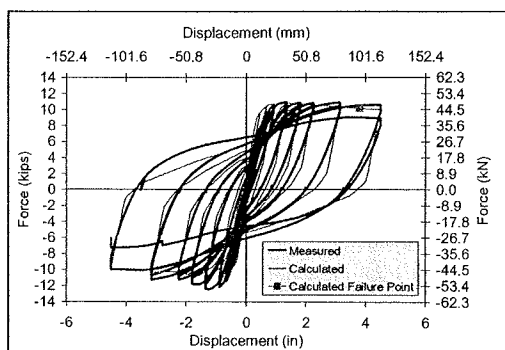


Figure 5-11: RSC Hysteresis Measured vs. Calculated

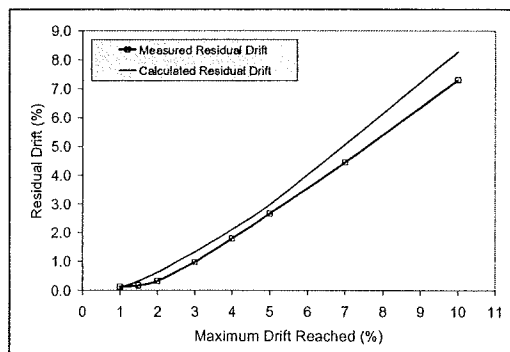


Figure 5-12: RSC Residual Drift: Measured vs. Calculated

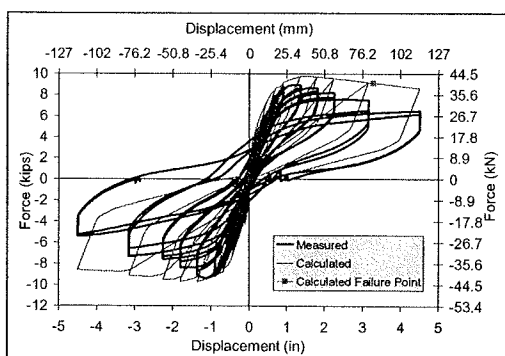


Figure 5-13: RNC Hysteresis Measured vs. Calculated

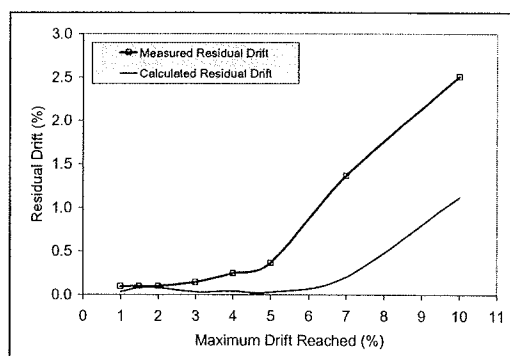


Figure 5-14: RNC Residual Drift: Measured vs. Calculated

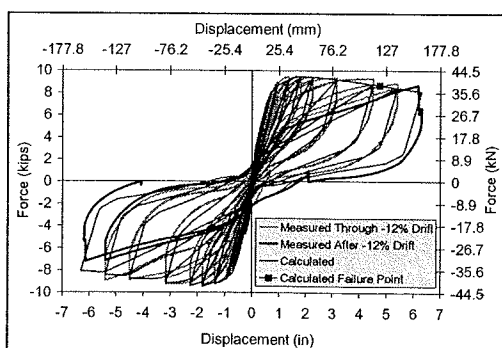


Figure 5-15: RNE Hysteresis Measured vs. Calculated

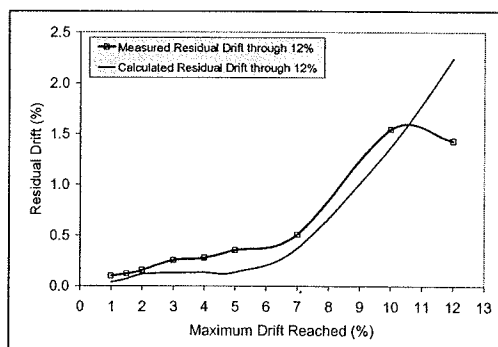


Figure 5-16: RNE Residual Drift: Measured vs. Calculated

## Appendix A

### Cost Comparison for Bridges with Conventional and Innovative Materials

Appendix A presents the cost comparison between two versions of a full-scale bridges, one with conventional concrete and reinforcing steel and the other with ECC and Nitinol in column plastic hinge zones.

With respect to cost competitiveness of SMA/ECC members, it should be noted that because these materials are new to civil engineering, their prices are not yet attuned to civil infrastructure applications. This is particularly true for SMAs, which are currently relatively expensive. This is in part because past applications of SMA materials have been mainly in sophisticated medical equipment or aerospace in which a small amount of material was used in expensive equipment. With more wide spread application of SMA in civil infrastructure, the price is expected be reduced. A similar trend was observed when fiber reinforced polymers began to be accepted for infrastructure use. Nonetheless an approximate cost comparison was made in subsequent sections based on current prices. Because of uncertainties in the timing of earthquakes, the time value of money was not accounted for.

The cost of Nitinol and ECC is higher than conventional reinforcing bars and concrete. However these materials will only be used in the plastic hinge regions of bridge columns. To compare the cost of an entire bridge incorporating Nitinol and ECC in column plastic hinge zones with a similar bridge incorporating conventional reinforcing bars and concrete, a typical bridge with the dimensions shown in Figure A-1 was considered.

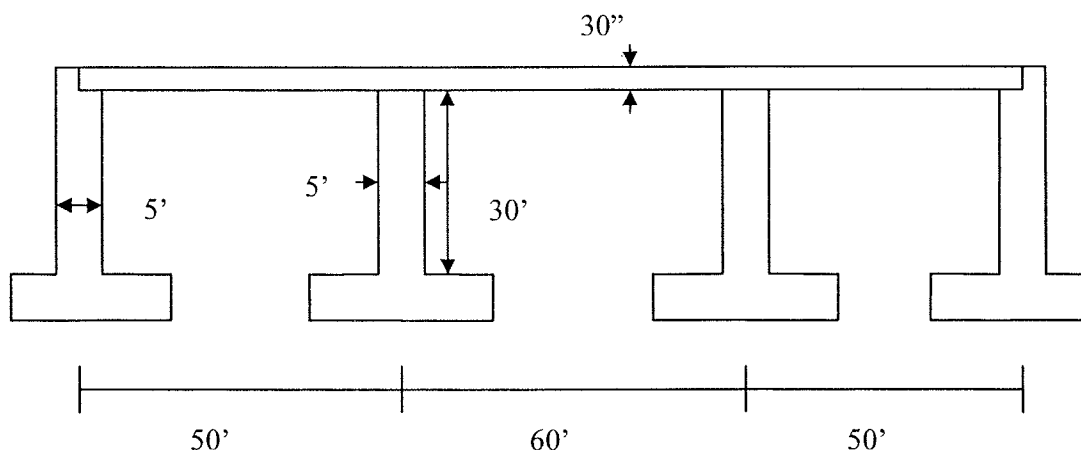


Figure A-1 – Typical Bridge Elevation

The width of the bridge deck is assumed to be 40'. The dimension of each pier foundation is 15'x15'x6' and the abutment foundation is 15'x40'x6'. The superstructure is a continuous slab and is supported on single column bents. The diameter of the columns is 5'. The reinforcing steel ratio in the deck, columns, and foundations are assumed to be 0.5%, 2% and 0.5% respectively. Table A-2 shows the amount of concrete and steel required for the bridge construction. Assuming that the plastic hinge height to be 6', the volume of ECC and Nitinol in column plastic hinge zones are calculated.

Table A-2- Materials Required for the Typical Bridge

	Deck (ft <sup>3</sup> )	Columns(ft <sup>3</sup> )	Abutments(ft <sup>3</sup> )	Foundations(ft <sup>3</sup> )	Total (ft <sup>3</sup> )
Concrete	16,000	1,178	12,000	9,900	39,078
Steel	80	24	240	50	394
ECC	-	236	-	-	236
Nitinol	-	4.72	-	-	4.72

Percentage of steel replaced by Nitinol =  $(4.72/394) * 100 = 1.2\%$

Percentage of concrete replaced by ECC =  $(236/39,078) * 100 = 0.6\%$

The price of Nitinol and ECC is assumed to be 50 and 20 times that of conventional steel and concrete, respectively. These ratios are based on the cost of limited purchase of materials in previous projects and are likely to be considerably lower when the volume is increased. Fifty percent of the total cost of the bridge construction is assumed for site preparation and formwork and 50% for the structure. Of the structure cost 60% is assumed for labor and 40% for material. Assuming steel and concrete unit prices as \$1250 per ton and \$80 per cubic yard, respectively, the total cost increase for the typical bridge will be approximately 7%. The reduction in the cost of SMA and ECC for higher volumes would change the increase perhaps to about 4 or 5%.

The initial bridge construction cost increase in the order of 5-7% is justifiable, since the bridge will be expected to remain operational for post disaster recovery operation and will need only minor repair. Survival of the bridge will also prevent indirect economical losses due to traffic delays and inconvenience to the public due to bridge closure.

The repair of damaged columns in conventionally reinforced concrete bridges will present additional life cycle cost. To estimate the repair cost, it is assumed that the columns will be repaired using steel jackets. The cost of steel jackets covering the full height of the columns is estimated at \$4 per lb, including material, fabrication, and installation. Taking the thickness of the jacket as 25.4 mm (1 in), the total weight of steel and cost are as follows:

Weight of the steel jackets =  $\{[(5*\pi)*1*30]/12\} * 2 * 490 = 38,485 \text{ lb}$

Cost of the steel jacketing =  $38,485 * 4 = \$ 153,940$

Additional costs due to excavation work, traffic control and safety measures are estimated at \$25,000, bringing the total repair cost to \$178,940. This is approximately 15% of the total bridge construction cost.

The above approximate estimates indicate that the use of the proposed new materials could be potentially cost-effective and lead to more cost effective and safer bridges.